

ALMA OBSERVATIONS OF THE SUBMILLIMETER DENSE MOLECULAR GAS TRACERS IN THE LUMINOUS TYPE-1 ACTIVE NUCLEUS OF NGC 7469

TAKUMA IZUMI¹, KOTARO KOHNO^{1,2}, SUSANNE AALTO³, AKIHIRO DOI⁴, DANIEL ESPADA^{5,6,7}, KAMBIZ FATHI⁸, NANASE HARADA⁹, BUNYO HATSUKADE⁶, TAKASHI HATTORI^{6,10}, PEI-YING HSIEH^{9,11}, SOH IKARASHI^{1,12}, MASATOSHI IMANISHI^{6,7,10}, DAISUKE IONO^{6,7}, SUMIO ISHIZUKI⁶, MELANIE KRIPS¹³, SERGIO MARTÍN¹³, SATOKI MATSUSHITA⁹, DAVID S. MEIER¹⁴, HIROSHI NAGAI⁶, NAOMASA NAKAI¹⁵, TAKU NAKAJIMA¹⁶, KOUICHIRO NAKANISHI^{5,6,7}, HIDEKO NOMURA¹⁷, MICHAEL W. REGAN¹⁸, EVA SCHINNERER¹⁹, KARTIK SHETH²⁰, SHURO TAKANO²¹, YOICHI TAMURA¹, YUICHI TERASHIMA²², TOMOKA TOSAKI²³, JEAN L. TURNER²⁴, HIDEKI UMEHATA¹, AND TOMMY WIKLIND⁵

¹ Institute of Astronomy, School of Science, The University of Tokyo, 2-21-1 Osawa, Mitaka, Tokyo 181-0015, Japan; takumaizumi@ioa.s.u-tokyo.ac.jp

² Research Center for the Early Universe, The University of Tokyo, 7-3-1 Hongo, Bunkyo, Tokyo 113-0033, Japan

³ Department of Earth and Space Sciences, Chalmers University of Technology, Onsala Observatory, SE-439 94 Onsala, Sweden

⁴ Institute of Space and Astronautical Science, 3-1-1 Yoshinodai, Chuo-ku, Sagami-hara 252-5210, Japan

⁵ Joint ALMA Observatory, Alonso de Córdova, 3107, Vitacura, Santiago 763-0355, Chile

⁶ National Astronomical Observatory of Japan, 2-21-1 Osawa, Mitaka, Tokyo 181-8588, Japan

⁷ SOKENDAI (The Graduate University for Advanced Studies), 2-21-1 Osawa, Mitaka, Tokyo 181-8588, Japan

⁸ Stockholm Observatory, Department of Astronomy, Stockholm University, AlbaNova Centre, SE-106 91 Stockholm, Sweden

⁹ Academia Sinica, Institute of Astronomy & Astrophysics, P.O. Box 23-141, Taipei 10617, Taiwan

¹⁰ Subaru Telescope, NAOJ, 650 North A'ohoku Place, Hilo, HI 96720, USA

¹¹ Institute of Astronomy, National Central University, No. 300, Jhongda Road, Jhongli City, Taoyuan County 32001, Taiwan, Republic of China

¹² European Southern Observatory, Karl-Schwarzschild-Strasse 2, D-85748 Garching, Germany

¹³ Institut de Radio Astronomie Millimétrique, 300 rue de la Piscine, Domaine Universitaire, F-38406 St. Martin d'Hères, France

¹⁴ Department of Physics, New Mexico Institute of Mining and Technology, 801 Leroy Place, Socorro, NM 87801, USA

¹⁵ Department of Physics, Faculty of Pure and Applied Sciences, University of Tsukuba, 1-1-1 Ten-nodai, Tsukuba, Ibaraki 305-8571, Japan

¹⁶ Solar-Terrestrial Environment Laboratory, Nagoya University, Furo-cho, Chikusa-ku, Nagoya 464-8601, Japan

¹⁷ Department of Earth and Planetary Sciences, Tokyo Institute of Technology, 2-12-1 Ookayama, Meguro, Tokyo 152-8550, Japan

¹⁸ Space Telescope Science Institute, 3700 San Marine Drive, Baltimore, MD 21218, USA

¹⁹ Max Planck Institute for Astronomy, Königstuhl 17, Heidelberg D-69117, Germany

²⁰ National Radio Astronomy Observatory, 520 Edgemont Road, Charlottesville, VA 22903, USA

²¹ Department of Physics, General Education, College of Engineering, Nihon University, Tamuramachi, Koriyama, Fukushima 963-8642, Japan

²² Department of Physics, Ehime University, 2-5 Bunkyo-cho, Matsuyama, Ehime 790-8577, Japan

²³ Department of Geoscience, Joetsu University of Education, Yamayashiki, Joetsu, Niigata 943-8512, Japan

²⁴ Department of Physics and Astronomy, UCLA, 430 Portola Plaza, Los Angeles, CA 90095-1547, USA

Received 2015 March 12; accepted 2015 August 16; published 2015 September 17

ABSTRACT

We present Atacama Large Millimeter/submillimeter Array (ALMA) Cycle 1 observations of the central kiloparsec region of the luminous type 1 Seyfert galaxy NGC 7469 with unprecedented high resolution ($0''.5 \times 0''.4 = 165 \times 132$ pc) at submillimeter wavelengths. Utilizing the wide bandwidth of ALMA, we simultaneously obtained HCN(4–3), HCO⁺(4–3), CS(7–6), and partially CO(3–2) line maps, as well as the 860 μ m continuum. The region consists of the central $\sim 1''$ component and the surrounding starburst ring with a radius of $\sim 1''.5$ – $2''.5$. Several structures connect these components. Except for CO(3–2), these dense gas tracers are significantly concentrated toward the central $\sim 1''$, suggesting their suitability to probe the nuclear regions of galaxies. Their spatial distribution resembles well those of centimeter and mid-infrared continuum emissions, but it is anticorrelated with the optical one, indicating the existence of dust-obscured star formation. The integrated intensity ratios of HCN(4–3)/HCO⁺(4–3) and HCN(4–3)/CS(7–6) are higher at the active galactic nucleus (AGN) position than at the starburst ring, which is consistent with our previous findings (submillimeter-HCN enhancement). However, the HCN(4–3)/HCO⁺(4–3) ratio at the AGN position of NGC 7469 (1.11 ± 0.06) is almost half of the corresponding value of the low-luminosity type 1 Seyfert galaxy NGC 1097 (2.0 ± 0.2), despite the more than two orders of magnitude higher X-ray luminosity of NGC 7469. But the ratio is comparable to that of the close vicinity of the AGN of NGC 1068 (~ 1.5). Based on these results, we speculate that some heating mechanisms other than X-ray (e.g., mechanical heating due to an AGN jet) can contribute significantly for shaping the chemical composition in NGC 1097.

Key words: galaxies: active – galaxies: individual (NGC 7469) – galaxies: ISM – ISM: molecules

1. INTRODUCTION

Investigation of the distribution, kinematics, and mass of dense molecular material in the centers of galaxies plays a key role in studying the evolution of galaxies because it is the reservoir of fuel for active galactic nuclei (AGNs) and also the site of massive star formation. On the other hand, these heating sources significantly affect their surrounding gas in radiative

and/or mechanical ways. For example, intense UV radiation from massive stars forms photodissociation regions (PDRs) around them, and X-ray-dominated regions (XDRs), which can be larger in volume than PDRs, are formed in the vicinity of AGNs (e.g., Maloney et al. 1996; Hollenbach & Tielens 1999; Meijerink & Spaans 2005; Meijerink et al. 2007). Cosmic rays from frequent supernovae (SNe) and the injection of mechanical energy due to SNe or AGN jet/outflow (mechanical

heating) are also important for the chemical layout (e.g., Meijerink et al. 2011; Kazandjian et al. 2012, 2015; Matsushita et al. 2015). Thus, the dense molecular gas can provide us critical information on the nature of the underlying physical processes accompanying the nonthermal radiation in the centers of galaxies.

Millimeter/submillimeter spectroscopic observations are indispensable for such a study since they can trace dense, cold molecular material with little dust extinction, which takes the bulk of gas mass in the nuclear regions of galaxies. This would contrast with observations of warm molecular gas such as H_2 1–0 S(1) in the near-IR (NIR; e.g., Hicks et al. 2009).

Nevertheless, our knowledge on the circumnuclear dense molecular matter has still been limited, especially for AGNs. This is because there have been only a small number of high-resolution (i.e., ~ 100 pc or higher scale) and sensitive observations of dense molecular gas even in nearby AGNs (e.g., García-Burillo et al. 2010; Krips et al. 2011; Sani et al. 2012; Matsushita et al. 2015), although several low-resolution surveys of dense gas have been conducted with single-dish telescopes to address their global properties (e.g., Gao & Solomon 2004a, 2004b).

This situation is now being improved significantly by the advent of the Atacama Large Millimeter/submillimeter Array (ALMA). Indeed, the spatial distribution, kinematics, and chemistry have been reported in greater detail for, e.g., NGC 1068 (García-Burillo et al. 2014; Takano et al. 2014; Viti et al. 2014; Nakajima et al. 2015), NGC 1097 (Fathi et al. 2013; Izumi et al. 2013; Martín et al. 2015), NGC 1433 (Combes et al. 2013), and NGC 1566 (Combes et al. 2014). Among these works, Izumi et al. (2013, hereafter I13) suggested that HCN (4–3)/ HCO^+ (4–3) and HCN(4–3)/CS(7–6) integrated intensity ratios seem to be higher in AGNs than in starburst (SB) galaxies (submillimeter-HCN enhancement), although the number of the sample galaxies in I13 is few and the actual cause of the enhancement is not clear.

With the above things in mind, we here present the results of our high-resolution ALMA band 7 observations of submillimeter dense gas tracers toward the central kpc region of NGC 7469. Because NGC 7469 hosts a luminous type 1 AGN ($L_{2-10\text{keV}} = 1.5 \times 10^{43} \text{ erg s}^{-1}$; Liu et al. 2014), we can investigate the effects of AGN luminosity on the surrounding molecular gas with little uncertainty by directly comparing the results with those obtained in the type 1 low-luminosity ($L_{2-10\text{keV}} = 6.9 \times 10^{40} \text{ erg s}^{-1}$; Liu et al. 2014) AGN, NGC 1097 (I13).

1.1. The Target Galaxy NGC 7469

NGC 7469 is an active galaxy with a large-scale (several kiloparsec) stellar bar detected at NIR wavelength (Knäpen et al. 2000). This galaxy is located at a distance of 70.1 Mpc ($z = 0.0164$; Meixner et al. 1990) and thus $1'' = 330$ pc, and it hosts a luminous type 1 Seyfert nucleus as evidenced by broad Balmer emission lines (FWHM of $\text{H}\beta = 4369 \text{ km s}^{-1}$; Peterson et al. 2014) with time variability (e.g., Bonatto & Pastoriza 1990; Collier et al. 1998). Time variability is also confirmed by UV and X-ray observations (e.g., Kriss et al. 2000; Nandra et al. 2000; Petrucci et al. 2004; Scott et al. 2005), revealing that this nucleus is indeed an AGN. NGC 7469 is also classified as a luminous infrared galaxy (LIRG) owing to its high IR luminosity ($L_{8-1000} \equiv L_{\text{IR}} = 10^{11.7} L_{\odot}$; Sanders et al. 2003).

The type 1 AGN is surrounded by a luminous circumnuclear SB ring with a radius of $1''.5-2''.5$ or 495–825 pc (e.g., Soifer et al. 2003; Díaz-Santos et al. 2007; see also Figure 1(a)), which accounts for two-thirds of the bolometric luminosity of the galaxy (Genzel et al. 1995). Therefore, this galaxy provides us with a nice opportunity to investigate how AGNs and SBs influence their surrounding molecular gas when observed at high resolution.

The SB ring is prominent at various wavelengths, including centimeter (Condon et al. 1991; Wilson et al. 1991; Orienti & Prieto 2010), far-IR (FIR; Papadopoulos & Allen 2000), mid-IR (MIR; Soifer et al. 2003; Gorjian et al. 2004), NIR (Genzel et al. 1995), optical to UV (Malkan et al. 1998; Díaz et al. 2000; Díaz-Santos et al. 2007), and soft X-ray (Perez-Olea & Colina 1996). A tidal interaction with its neighbor IC 5283 (~ 1.3 away from NGC 7469) is believed to have caused the powerful SB activity (e.g., Marquez & Moles 1994; Genzel et al. 1995). Dusty, young (< 100 Myr), and massive star clusters (individual typical mass is $10^{6-7} M_{\odot}$) exist within the ring (e.g., Díaz-Santos et al. 2007).

As for the central $\sim 1''$ region, multiwavelength studies including centimeter, K -band ($2.2 \mu\text{m}$), and $3.3 \mu\text{m}$ PAH features indicate that the AGN is energetically dominant at these wavelengths (Genzel et al. 1995; Lonsdale et al. 2003; Imanishi & Wada 2004), although one-third of the K -band continuum is of stellar origin (Genzel et al. 1995). A core jet-like structure (e.g., Lonsdale et al. 2003; Alberdi et al. 2006) and ionized outflows (Scott et al. 2005; Blustin et al. 2007) have also been observed in this AGN. Reverberation mapping revealed the mass of the central supermassive black hole (M_{BH}) to be $\sim 1 \times 10^7 M_{\odot}$ (Peterson et al. 2004, 2014). This M_{BH} is typical for QSOs at $z = 5$ on average, which will eventually grow to $M_{\text{BH}} = 10^9 M_{\odot}$ at $z = 0$ (Shankar et al. 2009). In addition, the Eddington ratio of this AGN (~ 0.3 ; Petrucci et al. 2004) is also comparable to those of QSOs. Therefore, the obtained spectrum of NGC 7469 could serve as a local template for high-redshift QSOs as well. Other relevant properties of NGC 7469 are summarized in Table 1 with the information shown above.

Observations of CO molecules revealed the existence of a large amount of cold molecular gas (e.g., Sanders et al. 1988; Meixner et al. 1990; Israel 2009), as well as warm molecular gas (Rosenberg et al. 2015), in the central region of NGC 7469. The detailed spatial structure and the dynamics of the cold molecular gas were first investigated by high-resolution ($0''.7$) CO(2–1) observations (Davies et al. 2004). Their CO(2–1) map also showed a ring-like structure, with a similar radius to that seen at other wavelengths, and a bright extended ($\sim 1''$) nuclear region. Note that we hereafter call this kind of (100 pc scale) central molecular concentration a circumnuclear disk (CND) in general. Davies et al. (2004) also found a bar or a pair of spiral arms between the ring and the CND, which is only visible in the molecular emission, and not prominent at NIR wavelengths. This configuration is quite unusual (see Section 5). The total molecular gas mass inside the $r < 2''.5$ (825 pc) region inferred from their observations is $2.7 \times 10^9 M_{\odot}$. The spatial distributions of typical dense gas tracers such as HCN and HCO^+ , on the other hand, have not been clear owing to the lack of spatial resolution of previous studies.

In this paper, we present the spatial distribution and line ratios of submillimeter dense gas tracers based on our high-resolution ($0''.50 \times 0''.40$, $1'' = 330$ pc) ALMA observations

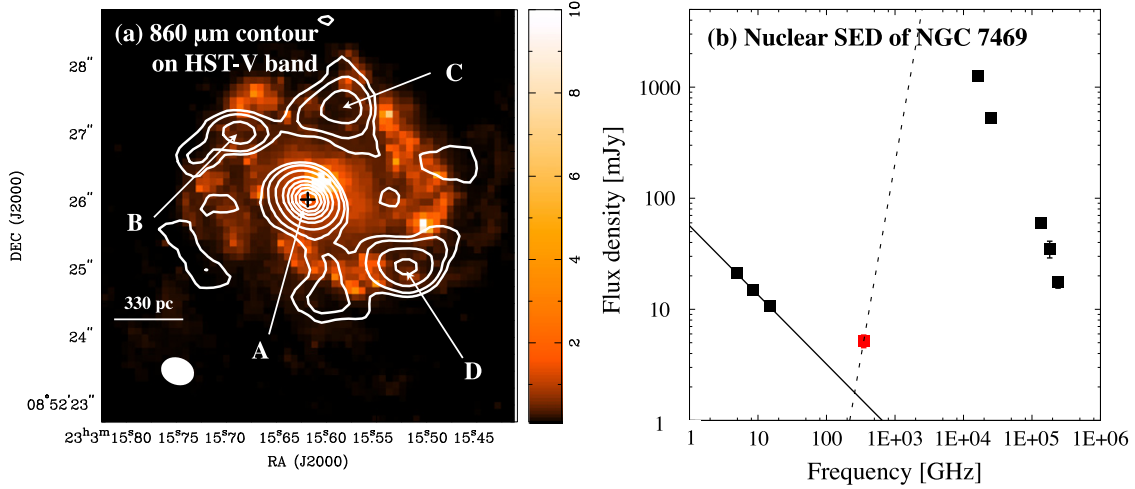


Figure 1. (a) Continuum map toward the central 2 kpc region of NGC 7469 at $860\ \mu\text{m}$ (contours) overlaid on the *HST* V-band (F550M) map (color; the intensity scale only indicates the counts). Contours are 3σ , 5σ , 10σ , 20σ , 30σ , 40σ , and 50σ , where $1\sigma = 0.09\ \text{mJy beam}^{-1}$. The maximum is $5.19\ \text{mJy beam}^{-1}$. The central plus sign indicates the peak position of the VLA 8.4 GHz continuum (Condon et al. 1991), which is identical to that of the $860\ \mu\text{m}$ continuum. We regard this position as that of the AGN. The white filled ellipse indicates the synthesized beam at $860\ \mu\text{m}$ ($0''.50 \times 0''.40$, PA = $68^\circ.6$). The AGN position and three bright knots in the SB ring are marked as A, B, C, and D, respectively. (b) Nuclear SED of the continuum emission in NGC 7469. We used 4.9 GHz data from Wilson et al. (1991), 8.4 and 14.9 GHz data from Orienti & Prieto (2010), our ALMA band 7 data (red square), 18.7 and 11.8 μm data from Reunanen et al. (2010), and *J*-, *H*-, and *K*-band data from Genzel et al. (1995). The solid and dashed lines indicate ν^α and $\nu^{2+\beta}$ scalings with $\alpha = -0.62$ and $\beta = 1.5$, respectively. The systematic flux errors are included in this plot.

Table 1
Properties of NGC 7469

Parameter	Value ^a	Reference ^b
RC3 morphology	(R')SAB(rs)a	(1)
Position of the nucleus		(1)
$\alpha_{\text{J2000.0}}$	$23^{\text{h}}03^{\text{m}}15^{\text{s}}.6$	
$\delta_{\text{J2000.0}}$	$+08^\circ52'26''.4$	
Position angle ($^\circ$)	128	(2)
Inclination angle ($^\circ$)	45	(2)
Recession velocity (km s^{-1})	4925 ($z = 0.0164$)	(3)
Adopted distance (Mpc)	70.1	
Linear scale (pc arcsec^{-1})	330	
Nuclear activity	Seyfert 1	(4)
$L_{2-10\ \text{keV}}$ (erg s^{-1})	1.5×10^{43}	(5)
L_{IR} (L_\odot)	2.5×10^{11}	(6)
$\langle \text{SFR} \rangle$ (CND) ($M_\odot \text{ yr}^{-1} \text{ kpc}^{-2}$)	50–100	(7)
Stellar age (CND) (Myr)	110–190	(7)

Notes.

^a The LSR velocity of the center of the galaxy is obtained from the CO(1–0) emission. We use this value to calculate the distance to NGC 7469 and the linear scale, by assuming $H_0 = 71\ \text{km s}^{-1} \text{ Mpc}^{-1}$, $\Omega_M = 0.27$, and $\Omega_\Lambda = 0.73$ cosmology. The $\langle \text{SFR} \rangle$ (CND) indicates the averaged star formation rate over the central $\sim 1''$ region (i.e., circumnuclear disk = CND). The stellar age is also for the CND.

^b (1) NASA/IPAC Extragalactic Database (NED; <http://ned.ipac.caltech.edu>); (2) Davies et al. (2004); (3) Meixner et al. (1990); (4) Osterbrock & Martel (1993); (5) Liu et al. (2014); (6) Sanders et al. (2003); (7) Davies et al. (2007).

of the central kiloparsec region of NGC 7469 involving HCN (4–3), $\text{HCO}^+(4-3)$, CS(7–6), and partially CO(3–2) lines and the underlying continuum emission. Our new ALMA observations improved this situation; we clearly separated the CND from the SB ring and then obtained a spectrum of each component. The spatial resolution of this study ($0''.5$) is comparable to that of the CO(2–1) observation ($0''.7$) by Davies et al. (2004), so that we can directly compare the molecular gas

distributions and kinematics. Note that, however, the spatial resolution of this study ($\sim 150\ \text{pc}$) would still be insufficient to exclusively probe the region where gas heating due to an AGN with NGC 7469-like luminosity dominates (see Appendix A for details).

We describe in Section 2 the details of our observations. An $860\ \mu\text{m}$ continuum map and a nuclear spectral energy distribution (SED) are shown in Section 3. A full band 7 spectrum and some line ratios are presented in Section 4, although we will extensively compare the line ratios with those obtained in other galaxies and discuss the possible causes of the HCN enhancement in our succeeding paper (Izumi et al. 2015). The spatial distributions of the submillimeter dense gas tracers are shown in Section 5. Finally, our main conclusions are summarized in Section 6. A kinematic study using our data is presented in Fathi et al. (2015).

2. OBSERVATION AND DATA REDUCTION

2.1. ALMA Band 7 Data of NGC 7469

NGC 7469 was observed with ALMA on 2013 November 3–4 with 28 antennas in C32-2 configuration, as a Cycle 1 early science program (ID = 2012.1.00165.S, PI = T. Izumi). Baseline lengths range from 15.0 to 1284.3 m (corresponds to the uv distance from 17.4 to 1493.4 $\text{k}\lambda$ at $860\ \mu\text{m}$). The observations were conducted in a single pointing with an $18''$ field of view, which fully covered the nucleus and the SB ring (total $\sim 4''$ in diameter). We set the phase tracking center to $(\alpha_{\text{J2000.0}}, \delta_{\text{J2000.0}}) = (23^{\text{h}}03^{\text{m}}15^{\text{s}}.64, +08^\circ52'25''.80)$. The receiver was tuned to cover the redshifted lines of HCN(4–3) (rest frequency $\nu_{\text{rest}} = 354.505\ \text{GHz}$), $\text{HCO}^+(4-3)$ ($\nu_{\text{rest}} = 356.734\ \text{GHz}$) in the upper side band (USB) and CS(7–6) ($\nu_{\text{rest}} = 342.883\ \text{GHz}$), CO(3–2) ($\nu_{\text{rest}} = 345.796\ \text{GHz}$) in the lower side band (LSB), both in the 2SB dual-polarization mode. Each spectral window has a bandwidth of 1.875 GHz, and two spectral windows were set to each sideband to achieve a total frequency coverage of $\sim 7.5\ \text{GHz}$. The velocity spacing

was originally 0.43 km s^{-1} (488 kHz) per channel, but 47 channels were binned to improve the signal-to-noise ratio, which resulted in a final velocity resolution of $\sim 20 \text{ km s}^{-1}$. In the following, we express velocities in the optical convention. Note that we could only cover the CO(3–2) line with $V_{\text{LSR}} > 4900 \text{ km s}^{-1}$ owing to the limited bandwidth for ALMA Cycle 1 observations, the recession velocity (4925 km s^{-1} , defined by CO(1–0) observations; Meixner et al. 1990), and the molecular line width of NGC 7469 (typically FWHM $\sim 200 \text{ km s}^{-1}$ at the nucleus). The bandpass, phase, and flux were calibrated with 3C 454.3, J2257+0743 (this object is 2° away from NGC 7469), and J2232+117, respectively. Weather conditions were good throughout the observations, with system temperatures of 100–200 K (usually 100–150 K). The total on-source integration time was ~ 55 minutes.

The reduction and calibration of the data were done with CASA version 4.1 (McMullin et al. 2007) in standard manners, and the data were delivered to us from the East Asia ALMA Regional Center. All images of the line and continuum emissions were reconstructed with the CASA task CLEAN (gain = 0.1, threshold = 1.0 mJy, weighting = natural). These images were further analyzed with MIRIAD (Sault et al. 1995). The achieved synthesized beams were typically $0''.50 \times 0''.40$, corresponding to $165 \text{ pc} \times 132 \text{ pc}$ ($\sim 150 \text{ pc}$ for the geometric mean) at the assumed distance of NGC 7469. The rms noise in the line channel maps is $0.55\text{--}0.58 \text{ mJy beam}^{-1}$ at a velocity resolution of 20 km s^{-1} after a primary beam correction and measured at areas free of line emission. However, in channels including CO(3–2) emission, the rms increases to $\sim 2.3 \text{ mJy beam}^{-1}$, probably as a result of the remaining sidelobes. For the continuum emission, the channels free of line emission were averaged, which resulted in an rms of $0.09 \text{ mJy beam}^{-1}$ centered at $\nu_{\text{rest}} = 349.7 \text{ GHz}$ ($860 \mu\text{m}$), after combining both the LSB and USB data. This continuum emission was subtracted in the uv -plane before making line maps. The conversion factors between Jy beam^{-1} and K are 51.50, 51.60, 50.47, and 51.83 K (Jy beam^{-1}) $^{-1}$ for CS(7–6), CO(3–2), HCN(4–3), and HCO⁺(4–3), respectively.

We used the MIRIAD task MOMENT to make the integrated intensity maps presented in Section 5, by computing the zeroth moment of each data cube without any clipping. The velocity range included for the integration was $\sim 4650\text{--}5250 \text{ km s}^{-1}$ for CS(7–6), HCN(4–3), and HCO⁺(4–3), but the lower limit was 4900 km s^{-1} for CO(3–2) owing to our spectral setting restrictions. These velocity ranges can cover the whole spectral range obtained within our $18''$ field of view, except for CO(3–2). Throughout this paper, the pixel scale of ALMA images is set to $0''.1$, and the displayed errors indicate only statistical ones unless mentioned otherwise. We use line intensities corrected for the primary beam attenuation for quantitative discussions. But this correction is not critical since most of the emission is within $\sim 4''$. The adopted systematic error of the absolute flux calibration was 10%.²⁵

2.2. Ancillary Data

We retrieved the *Hubble Space Telescope* (*HST*) Advanced Camera for Surveys/HRC image (F550M) of NGC 7469 from the Hubble Legacy Archive.²⁶ This image was calibrated by the

HST pipeline products in a standard manner. We used the image only to check the positional consistency or shift between peaks in optical (*V* band) and our ALMA band 7 images as shown in Section 3.

3. 860 μm CONTINUUM EMISSION

Figure 1(a) shows the $860 \mu\text{m}$ continuum emission overlaid on the *HST* *V*-band (F550M) emission in the central 2 kpc region of NGC 7469. In this figure, we can see a bright central source, which corresponds to the CNB as defined in Section 1.1, and some knots in the SB ring with a radius of $\sim 1''.5$ ($\sim 500 \text{ pc}$). The peak position of the $860 \mu\text{m}$ continuum emission is $(\alpha_{\text{J2000.0}}, \delta_{\text{J2000.0}}) = (23^{\text{h}} 03^{\text{m}} 15^{\text{s}}.62, +08^{\circ}52'26''.04)$, which precisely coincides with that of the VLA 8.4 GHz (3.5 cm) continuum emission (Condon et al. 1991; Orienti & Prieto 2010; their angular resolutions were $0''.22\text{--}0''.25$). This precise match supports the accuracy of the astrometry of ALMA. We hereafter treat this peak position as the position of the AGN of NGC 7469. The $860 \mu\text{m}$ flux density there (marked as A in Figure 1(a)) is $5.19 \pm 0.09 \text{ mJy beam}^{-1}$. The $860 \mu\text{m}$ knots in the SB ring (marked as B, C, and D in Figure 1(a)) coincide with those visible at centimeter wavelengths (e.g., 8.4 GHz; Orienti & Prieto 2010) and the knots of dense molecular gas tracers such as CO(3–2), HCN(4–3), and HCO⁺(4–3) (Section 5). On the other hand, there is inconsistency between the peak positions of the $860 \mu\text{m}$ and those of the *V*-band emissions. The magnitude of this positional shift is $\sim 0''.5$, which is the same size as our synthesized beam and thus significant. Similar discrepancy was also reported between the PdBI CO(2–1) emission and *HST* *J*-band maps (Davies et al. 2004) and between centimeter and *J*-, *H*-, and *K*-band maps (Genzel et al. 1995), for example. Although one possible explanation for the discrepancy is that the absolute astrometry of *HST* is slightly off, it is rather likely that the stellar light is obscured by large amounts of dust traced by the $860 \mu\text{m}$ emission, as also suggested by Díaz-Santos et al. (2007).

We also investigated the origin (thermal or nonthermal) of the $860 \mu\text{m}$ continuum at position A by constructing the SED as shown in Figure 1(b). We used high angular resolution (comparable to, or higher than our ALMA band 7 resolution = $0''.5$) data of 4.9 GHz from Wilson et al. (1991), 8.4 and 14.9 GHz from Orienti & Prieto (2010), 11.8 and $18.7 \mu\text{m}$ from Reunanen et al. (2010), and *J*, *H*, and *K* bands from Genzel et al. (1995). The systematic flux uncertainty is included. Although the data are sparse at the submillimeter to FIR range, the SED indicates that the centimeter continuum emission can be well reproduced as synchrotron ($\alpha = -0.62 \pm 0.02$; flux $\propto \nu^\alpha$), whereas the flux density of the $860 \mu\text{m}$ continuum is well beyond the expected value of the synchrotron emission, i.e., the $860 \mu\text{m}$ continuum is dominated by thermal emission. Note that the percentage of the $860 \mu\text{m}$ continuum that is due to synchrotron is $\sim 30\%$ as estimated from the above scaling. In addition, we used the CLEAN algorithm to deconvolve the continuum emission in the LSB and USB of ALMA band 7 separately. Then, the flux at position A is $4.66 \pm 0.13 \text{ mJy beam}^{-1}$ and $5.00 \pm 0.13 \text{ mJy beam}^{-1}$ at 343.7 and 356.0 GHz, respectively (errors indicate statistical ones only since they were observed simultaneously), suggesting a positive spectral index ($\beta = 0 \pm 1$; flux $\propto \nu^{(2+\beta)}$), but the number of data points is just two for this fitting). Therefore, we conclude that the

²⁵ <https://almascience.eso.org/documents-and-tools/cycle-1/alma-proposers-guide>

²⁶ <http://hla.stsci.edu>

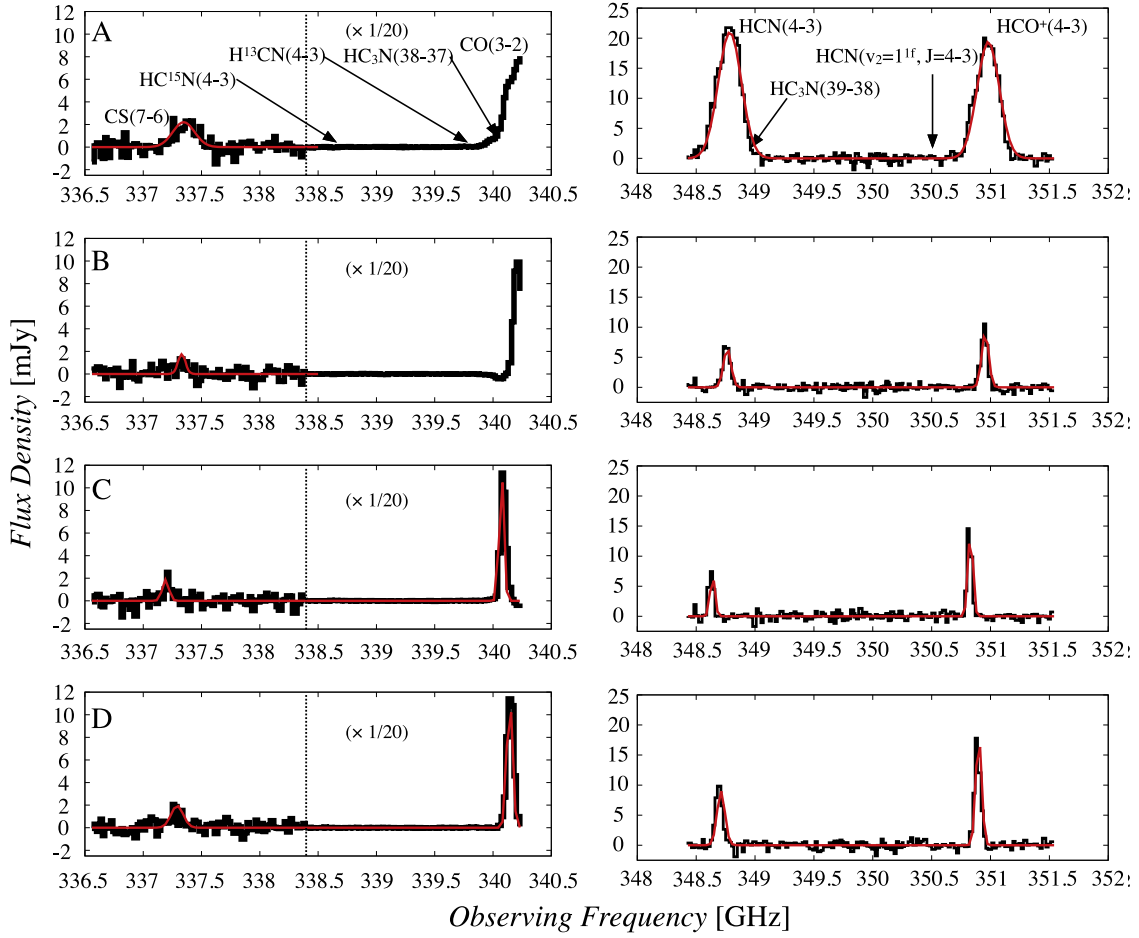


Figure 2. ALMA band 7 spectra extracted with a single synthesized beam (150 pc resolution) placed at positions A, B, C, and D in Figure 1(a). The flux of the spectral window containing CO(3–2) emission line is reduced by 20 times for a presentation. At position A (=AGN), we detected CO(3–2), HCN(4–3), HCO⁺(4–3), and CS(7–6) with $>3\sigma$ significance. Other lines were undetected (i.e., $<3\sigma$) or blended with other lines. Their expected locations are marked by black arrows in the top panel. The redshift of the nucleus assumed in this study is $cz = 4925 \text{ km s}^{-1}$, based on CO(1–0) observations (Meixner et al. 1990). The Gaussian fit to the observed CS(7–6), CO(3–2), HCN(4–3), and HCO⁺(4–3) emissions is represented by the red line. The fitting parameters can be found in Table 2. As for CO(3–2), we could not cover the whole spectral range in our observations. Thus, we use the peak flux density in the channel map (Figure 3) and the FWHM of the HCN(4–3) emission line, to anyhow fit the CO(3–2) emission. However, we did not fit the CO(3–2) emission line at positions A and B, since we could not find a clear turnover feature or blue part of the spectrum there. The continuum emission has been subtracted. Note that there is a dip at the lower-frequency side of the CO(3–2) emission line at position B, which is due to a negative sidelobe (see also Figure 3).

860 μm continuum at position A mainly originates from thermal dust.

4. BAND 7 SPECTRA, LINE RATIOS, AND DENSE MOLECULAR GAS MASS

Here we show the ALMA band 7 spectra in Figure 2. These spectra were extracted from a single synthesized beam (150 pc resolution) placed at positions A–D in Figure 1(a), for comparison. The strongest line at position A is CO(3–2), followed by HCN(4–3), HCO⁺(4–3), and CS(7–6). Other lines were not detected (i.e., $<3\sigma$) or are blended with other lines, and their spectral positions are marked by black arrows in Figure 2. On the other hand, at the SB ring (positions B–D), HCO⁺(4–3) is brighter than HCN(4–3). The FWHM of the HCN(4–3) and HCO⁺(4–3) emissions is 200 and 190 km s^{-1} , 66 and 60 km s^{-1} , 41 and 42 km s^{-1} , and 50 and 50 km s^{-1} at positions A–D, respectively (see also Figures 4 and 5). Thus, these values are consistent with each other, which suggests that they are tracing the same volume. We list the emission-line

parameters at these positions in Table 2 with other relevant quantities.

4.1. $R_{\text{HCN}/\text{HCO}^+}$ and $R_{\text{HCN}/\text{CS}}$

By inspecting the spectra, one may notice that the HCN(4–3)/HCO⁺(4–3) integrated intensity ratio (hereafter $R_{\text{HCN}/\text{HCO}^+}$) is higher than unity only at position A. To further clarify this, we list the values of $R_{\text{HCN}/\text{HCO}^+}$, and the HCN(4–3)/CS(7–6) integrated intensity ratio (hereafter $R_{\text{HCN}/\text{CS}}$; I13 also proposed this ratio to be an empirical discriminator of AGNs and SBs) at positions A–D in Table 3. The integrated intensity of each line emission at each position is given in Table 2. They are calculated by the Gaussian fit to the data. The line ratios in Table 3 are consistent with the submillimeter-HCN enhancement scenario first proposed by I13, i.e., AGNs tend to show higher $R_{\text{HCN}/\text{HCO}^+}$ and/or $R_{\text{HCN}/\text{CS}}$ compared to SB galaxies, although the $R_{\text{HCN}/\text{HCO}^+}$ at position A is only slightly larger than unity and totally comparable to the $R_{\text{HCN}/\text{HCO}^+}$ of a typical early phase (e.g., Martín et al. 2009) SB galaxy NGC 253 (1.1 ± 0.3 ; I13). But the ratio is

Table 2
Parameters of Detected Lines at the Peak Positions of the 860 μm Continuum Emission

Emission	ν_{rest} (GHz)	n_{crit} (cm^{-3})	E/k_{B} (K)	Peak Flux (mJy beam $^{-1}$)	v_{LSR} (km s^{-1})	Δv (km s^{-1})	S (Jy beam $^{-1}$ km s $^{-1}$)	I (K km s $^{-1}$)
(1)	(2)	(3)	(4)	(5)	(6)	(7)	(8)	(9)
CS($J = 7-6$)	342.883	2.9×10^6	65.8	2.20 ± 0.58	4919.7 ± 29.3	196.5 ± 27.2	0.46 ± 0.14	23.7 ± 7.1
				$<1.74^{\text{a}}$	$<0.12^{\text{c}}$	$<6.2^{\text{c}}$
				1.87 ± 0.58	5059.9 ± 60.6	59.0 ± 18.0	$0.12 \pm 0.05^{\text{d}}$	$6.0 \pm 2.6^{\text{d}}$
				1.98 ± 0.58	4982.2 ± 47.9	74.1 ± 17.0	$0.16 \pm 0.06^{\text{d}}$	$8.0 \pm 3.0^{\text{d}}$
CO($J = 3-2$)	345.796	8.4×10^3	33.2
				$202 \pm 2^{\text{b}}$
				$232 \pm 2^{\text{b}}$	$9.7 \pm 1.2^{\text{c}}$	$498.9 \pm 61.0^{\text{c}}$
				$235 \pm 2^{\text{b}}$	$12.0 \pm 0.4^{\text{c}}$	$617.5 \pm 19.2^{\text{c}}$
HCN($J = 4-3$)	354.505	8.5×10^6	42.5	21.00 ± 0.55	4915.8 ± 7.8	199.6 ± 6.7	4.46 ± 0.19	225.1 ± 9.5
				6.41 ± 0.55	4935.0 ± 17.5	65.5 ± 5.9	0.45 ± 0.06	22.6 ± 2.8
				6.84 ± 0.55	5044.2 ± 26.5	41.0 ± 5.0	0.30 ± 0.04	15.0 ± 2.0
				8.98 ± 0.55	4981.3 ± 16.3	50.1 ± 1.5	0.48 ± 0.03	24.2 ± 1.7
HCO $^+$ ($J = 4-3$)	356.734	1.8×10^6	42.8	19.38 ± 0.58	4914.1 ± 5.7	189.7 ± 4.8	3.91 ± 0.15	202.8 ± 7.9
				9.09 ± 0.58	4936.6 ± 13.0	60.3 ± 3.9	0.58 ± 0.05	30.2 ± 2.7
				14.50 ± 0.58	5045.2 ± 8.9	41.5 ± 1.9	0.64 ± 0.04	33.2 ± 2.0
				18.24 ± 0.58	4984.4 ± 6.1	50.1 ± 1.5	0.97 ± 0.04	50.4 ± 2.2
860 μm	349.7	5.19 ± 0.09
				1.04 ± 0.09
				1.23 ± 0.09
				1.70 ± 0.09

Notes. Column 1: full line name. Column 2: line rest frequency. Column 3: critical density of the line, calculated for $T_{\text{kin}} = 100$ K in the optically thin limit (Greve et al. 2009). Column 4: upper-level energy. Column 5: peak flux density of the line and continuum emission determined from the Gaussian fits to the data (Figure 2). They are extracted with a single synthesized beam (150 pc resolution) placed at positions A (AGN position), B, C, and D (listed vertically in this order) marked in Figure 1(a). For the lines, errors were estimated from the adjacent emission-free channels except for CO(3–2). For the continuum, an error was estimated from the emission-free areas in the continuum image. The primary beam attenuation is corrected. Columns 6 and 7: LSR velocity and FWHM of the line, which is calculated by the Gaussian fit. Columns 8 and 9: velocity-integrated intensity in the unit of (Jy beam $^{-1}$ km s $^{-1}$) and (K km s $^{-1}$) at the same positions as listed in Column 5, which is estimated by combining Columns 5 and 7.

^a The 3σ upper limit is listed.

^b The peak flux density (i.e., flux density at the turnover feature) in the channel map is listed. Thus, these are not the results of the Gaussian fit to the data.

^c The velocity centroid and the FWHM of HCN(4–3) at the corresponding position are used for the Gaussian fits.

^d Although the resultant integrated intensity is $<3\sigma$, we list the value.

Table 3
HCN(4–3)/HCO $^+$ (4–3), HCN(4–3)/CS(7–6), and HCN(4–3)/CO(3–2)
Integrated Intensity Ratios in NGC 7469

Position	A	B	C	D
$R_{\text{HCN}/\text{HCO}^+}$	1.11 ± 0.06	0.75 ± 0.11	0.45 ± 0.07	0.48 ± 0.04
$R_{\text{HCN}/\text{CS}}$	9.50 ± 2.87	>3.65	2.50 ± 1.13	3.03 ± 1.15
$R_{\text{HCN}/\text{CO}}$ ^a	0.03 ± 0.01	0.04 ± 0.01

Note. Row 1: the positions marked in Figure 1(a), where line ratios are extracted with a single synthesized beam (150 pc resolution). Row 2: HCN(4–3)/HCO $^+$ (4–3) integrated intensity ratio. Row 3: HCN(4–3)/CS(7–6) integrated intensity ratio. Row 4: HCN(4–3)/CO(3–2) integrated intensity ratio (tentative). The integrated intensities of these lines are shown in Table 2, although the values of CO(3–2) are tentative. The velocity ranges integrated over are shown in Section 2. The ratios are measured in the brightness temperature scale.

^a The peak intensity ratio at position B is ~ 0.03 .

significantly higher than that of a typical late-phase (e.g., Martín et al. 2009) SB galaxy, M82 ($R_{\text{HCN}/\text{HCO}^+} \sim 0.4$; I13). Note that a mechanical heating due to, e.g., frequent SNe would be responsible in the central region of NGC 253 (Rosenberg et al. 2014a) for its relatively high $R_{\text{HCN}/\text{HCO}^+}$, as compared to M82.

By investigating the 8.4 GHz radio flux obtained at 0''2 (Colina et al. 2001) and at 0''03, Davies et al. (2007) estimated

that a nuclear SN rate is $\sim 0.1 \text{ yr}^{-1}$. This rate corresponds to a star formation rate of $\sim 15 M_{\odot} \text{ yr}^{-1}$ assuming the Salpeter initial mass function (Salpeter 1955). Our relatively large spatial resolution (~ 150 pc) would pick up line fluxes emanating from the extended SB activity inside the CND (see also Appendix A for the estimated size of the XDR of NGC 7469), which would impact the line ratios discussed here. We cannot find any morphological and kinematic signatures of a jet–ISM interaction in the high-resolution maps of H $_2$ and Br γ emissions (Hicks et al. 2009; Müller-Sánchez et al. 2011), although Lonsdale et al. (2003) reported the existence of a core radio jet-like structure. Therefore, we speculate that the energetics of the CND of NGC 7469 is influenced by both the AGN (XDR) and the SB activity (PDR) when observed at the rather coarse resolution (150 pc in this work).

In our succeeding paper (Izumi et al. 2015), we conducted non-local thermodynamic equilibrium (non-LTE) line modelings by the RADEX code (van der Tak et al. 2007). Assuming a one-zone cloud, we widely changed gas kinetic temperature, molecular column density, molecular abundance ratio, and background temperature (we expect higher background temperature in AGNs than in SB galaxies) but fixed H $_2$ gas density among the models ($n_{\text{H}_2} = 10^5 \text{ cm}^{-3}$). This treatment was based on the assumption that there would be no systematic variation in n_{H_2} between AGNs and SB galaxies. Then, we calculated the resultant line intensity ratio, i.e., $R_{\text{HCN}/\text{HCO}^+}$ or $R_{\text{HCN}/\text{CS}}$, in

each model case. As a result, we found that both $X(\text{HCN})/X(\text{HCO}^+) \gtrsim 10$ and $X(\text{HCN})/X(\text{CS}) \gtrsim 10$ are required to reproduce $R_{\text{HCN}/\text{HCO}^+} > 1$ and $R_{\text{HCN}/\text{CS}} > 10$ as are observed in NGC 7469 and NGC 1097. Furthermore, the line opacity of HCN(4–3) is moderately thick, whereas that of CS(7–6) is thin when $R_{\text{HCN}/\text{CS}} \gtrsim 10$. Here $X(\text{mol})$ indicates a molecular fractional abundance relative to H_2 . The above required abundance ratios are significantly higher (at least by a factor of a few) than those necessary to reproduce the line ratios in SB galaxies. Therefore, these results suggest that a chemical abundance variation between AGNs and SB galaxies would be the key for the HCN enhancement.

In the following, we discuss possible mechanisms to realize the abundance variation in AGNs, although it is still unclear, since (1) there are various ways to change the chemical compositions significantly (e.g., X-ray irradiation, mechanical heating, high-temperature chemistry), and (2) the number of high-resolution observational data of dense gas tracers is currently insufficient.

In conventional XDR models (Lepp & Dalgarno 1996; Meijerink & Spaans 2005), we find that reproducing a high $X(\text{HCN})/X(\text{HCO}^+)$ such as $\gtrsim 10$ is hard (usually it is less than unity), since a powerful ionizing capability in XDRs will favor enhancing ionic species such as HCO^+ . Nonetheless, according to the steady-state, gas-phase one-dimensional XDR models intensively presented by Meijerink & Spaans (2005) and Meijerink et al. (2007), we can expect a high $X(\text{HCN})/X(\text{HCO}^+)$ and the resultant $R_{\text{HCN}/\text{HCO}^+} > 1$ in a low to moderate gas density ($n_{\text{H}_2} \lesssim 10^5 \text{ cm}^{-3}$) cloud with a low hydrogen column density ($N_{\text{H}} \lesssim 10^{22.5} \text{ cm}^{-2}$) and a high X-ray flux (e.g., $F_{\text{X}} \gtrsim 10 \text{ erg s}^{-1} \text{ cm}^{-2}$). For larger N_{H} where the F_{X} is attenuated, they predicted $R_{\text{HCN}/\text{HCO}^+} < 1$. Following this scenario, we estimate that the largest distance from the AGN that can keep $F_{\text{X}} > 10 \text{ erg s}^{-1} \text{ cm}^{-2}$ is $r \sim 18 \text{ pc}$ and $\sim 35 \text{ pc}$ for NGC 1097 and NGC 7469, respectively, considering their 2–10 keV X-ray luminosities ($L_{2-10 \text{ keV}} = 6.9 \times 10^{40} \text{ erg s}^{-1}$ and $1.5 \times 10^{43} \text{ erg s}^{-1}$ for NGC 1097 and NGC 7469, respectively; Liu et al. 2014). We here assume that the X-ray emission is isotropic around the AGN itself. Attenuation due to obscuring material is considered for this estimation (Morrison & McCammon 1983; Appendix B). But one critically weak point in this scenario is that the model-predicted line intensities are extremely low (Meijerink et al. 2006, 2007), which is inconsistent with the prominent HCN(4–3) and $\text{HCO}^+(4-3)$ emission lines in these galaxies. Furthermore, Martín et al. (2015) argued that the HCN(1–0)/ $\text{HCO}^+(1-0)$ integrated intensity ratio is decreased in NGC 1097 as we approach the very central region (~ 2 at the edge of the CN, ²⁷ but ~ 1.5 at the center), which seems to be incompatible with the above speculation of the largest distance for a high line ratio in NGC 1097. Note that, however, Martín et al. (2015) did not fully resolve the CN of NGC 1097; thus, their argument is a tentative one at this moment.

Another possible scenario is the high-temperature gas-phase chemistry (Harada et al. 2010), which significantly enhances $X(\text{HCN})$ especially at $T > 300 \text{ K}$ owing to the activated formation path from CN (see also Figure 17 of I13). This mechanism would be important to make line intensity of HCN(4–3) sufficiently detectable. Furthermore, $X(\text{HCO}^+)$ will be somewhat decreased in these models since they will react with

H_2O (this is also a typical molecule in a high-temperature environment) to form H_3O^+ . This type of chemistry can be complementary to XDRs (Harada et al. 2013), where we can expect much higher gas temperature in such regions owing to efficient X-ray heating than in SB environments. Indeed, some fraction of warm molecular gas exists in NGC 7469, as evidenced by the detections of NIR H_2 (Hicks et al. 2009) and high- J CO emission lines (Rosenberg et al. 2015).

With these items, we here focus on the notable fact that the $R_{\text{HCN}/\text{HCO}^+}$ obtained at position A of NGC 7469 (1.11 ± 0.13) is only half that at the CN of NGC 1097 (2.0 ± 0.2 ; I13), despite the more than two orders of magnitude higher X-ray luminosity of NGC 7469. Note that NGC 1097 also hosts a nuclear SB activity in the CN ($\sim a \text{ few } M_{\odot} \text{ yr}^{-1}$; Davies et al. 2007), which would contaminate the line fluxes obtained with the $\sim 100 \text{ pc}$ resolution beam (I13). Furthermore, García-Burillo et al. (2014) found $R_{\text{HCN}/\text{HCO}^+} = 1.5$ at the vicinity of the AGN in NGC 1068 ($L_{2-10 \text{ keV}} = 6.9 \times 10^{42} \text{ erg s}^{-1}$; Panessa et al. 2006), whereas it increases to ~ 3 at the east/west knots of its CN, which are $\sim 100 \text{ pc}$ away from the AGN (their spatial resolution was $\sim 35 \text{ pc}$). These results indicate that higher X-ray luminosity does not simply lead to higher $R_{\text{HCN}/\text{HCO}^+}$. From the perspective of high-temperature chemistry, the results again seem to be controversial, since the large difference in X-ray luminosity would compensate the ~ 2.5 times larger spatial scale (in area) sampled in NGC 7469 than in NGC 1097, leading to a higher X-ray energy deposition rate per particle (this is an important parameter to determine the thermal structure of XDRs; e.g., Maloney et al. 1996) in NGC 7469, if the molecular gas distributes uniformly over the CN. In this case, we can expect a higher $R_{\text{HCN}/\text{HCO}^+}$ in NGC 7469 than in NGC 1097 by a naive view, but the actual result is totally opposite.

Therefore, we presume that a nonradiative heating, namely, mechanical heating caused by, e.g., an AGN jet or outflow, is important to realize the high $R_{\text{HCN}/\text{HCO}^+}$ of 2–3 (Kazandjian et al. 2012, 2015) as is observed in NGC 1097 and in the east/west knots of the CN of NGC 1068. Indeed, a large radio jet exists in NGC 1068, which is supposed to cause shocks in the knots (e.g., Krips et al. 2011). Furthermore, a radio core jet has been discovered in NGC 1097 (e.g., Mezcuca & Prieto 2014), although its intrinsic (deprojected) size is uncertain. However, we cannot discard the possibility that the line-emitting region of NGC 1097 is extremely centrally concentrated, which would result in a higher energy deposition rate per particle (i.e., more violent X-ray heating) than in NGC 7469 and the close vicinity of NGC 1068. Moreover, we again emphasize that the line fluxes of NGC 7469 would be contaminated by the emission from the extended SB region inside the CN. Higher-resolution observations of these molecular emissions are necessary to accurately map the distribution of the line ratios across the CN of NGC 1097 and NGC 7469 and to search for a signature of shock–ISM interaction.

4.2. Other Line Emissions and Their Ratios

Table 3 also includes HCN(4–3)/CO(3–2) integrated intensity ratios ($R_{\text{HCN}/\text{CO}}$) extracted at positions C and D. We exclude the ratio at positions A and B since we could not measure the accurate fluxes there. Admitting the uncertainty in CO(3–2) integrated intensity (we used the velocity centroid and the FWHM of the HCN(4–3) emission line to fit the Gaussian profile to the CO(3–2) line; see also Figure 2 and Table 2), the

²⁷ An upper limit of the image-convolved size is $\sim 90 \times 70 \text{ pc}$ (I13).

Table 4
HCN(4–3) and HCO⁺(4–3) Line Luminosities in Units of Both L_{\odot} and $\text{K km s}^{-1} \text{pc}^2$

Position	$L_{\text{HCN}(4-3)}$ (L_{\odot})	$L_{\text{HCO}^+(4-3)}$ (L_{\odot})	$L'_{\text{HCN}(4-3)}$ ($\text{K km s}^{-1} \text{pc}^2$)	$L'_{\text{HCO}^+(4-3)}$ ($\text{K km s}^{-1} \text{pc}^2$)
AGN	$(7.95 \pm 0.34) \times 10^3$	$(7.01 \pm 0.27) \times 10^3$	$(5.58 \pm 0.24) \times 10^6$	$(4.83 \pm 0.19) \times 10^6$
CND	$(2.10 \pm 0.09) \times 10^4$	$(1.86 \pm 0.08) \times 10^4$	$(1.47 \pm 0.06) \times 10^7$	$(1.28 \pm 0.06) \times 10^7$

Note. Row 1: line luminosities within a synthesized beam (150 pc resolution) placed at position A (i.e., AGN position) marked in Figure 1(a). The luminosity was calculated following the formulae by Solomon & Vanden Bout (2005). Row 2: line luminosities within the CND (i.e., the central $\sim 1'' = 330$ pc diameter region).

tentative $R_{\text{HCN}/\text{CO}}$ at the SB ring are well below the value obtained in Ori-KL (~ 0.32 ; Schilke et al. 1997). Since the line critical density is orders of magnitude different between HCN(4–3) and CO(3–2) (see Table 2), we can expect the line-emitting region of HCN(4–3) to be much smaller than that of CO(3–2). Hence, this ratio would be highly prone to be affected by the spatial resolution, which could lead to significantly lower $R_{\text{HCN}/\text{CO}}$ in NGC 7469 than in Ori-KL. This is well manifested in the case of NGC 253 (SB galaxy). When observed at ~ 200 – 300 pc resolution (comparable to our 150 pc resolution for NGC 7469), $R_{\text{HCN}/\text{CO}} \sim 0.03$ (Israel et al. 1995; Knudsen et al. 2007), which is quite similar to our result. However, the ratio increases to ~ 0.08 , i.e., an increase by a factor of a few, when observed at higher resolution (25–30 pc; Sakamoto et al. 2011). Then, matching the spatial resolution is important to compare line ratios of emission lines with totally different critical densities among objects.

We also found that the $\text{H}^{12}\text{CN}(4-3)/\text{H}^{13}\text{CN}(4-3)$ isotopic ratio at position A was $\gtrsim 11.9$ in the brightness temperature scale. Note that this is a peak intensity ratio and we used a 3σ upper limit for $\text{H}^{13}\text{CN}(4-3)$. Then, adopting a $^{12}\text{C}/^{13}\text{C}$ ratio of >40 observed in NGC 253 (Martín et al. 2010; Henkel et al. 2014), the upper limit to the opacity of the $\text{H}^{12}\text{CN}(4-3)$ is 3.5 at the position. For this calculation, we assume that (1) the gas is in the LTE, (2) H^{12}CN is optically thick, (3) H^{13}CN is optically thin, and (4) H^{12}CN and H^{13}CN emissions are coming from the same volume of gas. Alternatively, if we adopt a $^{12}\text{C}/^{13}\text{C}$ ratio of 100 obtained in Mrk 231 (Henkel et al. 2014, ~ 19 kpc resolution), the upper limit of the opacity increases to 8.8. In either case, the derived optical depth is rather smaller than the values of the Galactic star-forming regions (e.g., ~ 70 in Ori-KL; Schilke et al. 1997), likely reflecting the much more turbulent environments in the nuclear regions of galaxies.

Note that vibrationally excited HCN emission, namely, HCN($v_2 = 1^{\text{f}}, J = 4-3$) at $\nu_{\text{rest}} = 356.256$ GHz, was not detected at position A, despite the fact that NGC 7469 is classified as a LIRG (Sanders et al. 2003) hosting a luminous AGN. Considering the above-mentioned modest optical depth of $\text{H}^{12}\text{CN}(4-3)$, we can expect HCN($v_2 = 1^{\text{f}}, J = 4-3$) to be completely optically thin, which makes itself hard to detect. Therefore, the nondetection of HCN($v_2 = 1^{\text{f}}, J = 4-3$) emission does not necessarily mean that IR pumping has little contribution to the observed line intensities, although we here simply treat that the HCN(4–3) emission is the consequence of the purely rotational transition. We need quantitative modeling of the line excitation to further address this problem. We also note that the contribution of $\text{HC}_3\text{N}(39-38)$ emission to the HCN(4–3) emission is negligible at position A since HC_3N emission is typically much fainter than that of HCN, and the line profile of the bluer HCN(4–3) is very similar to that of $\text{HCO}^+(4-3)$, which does not suffer from line blending. We thus

conclude that the contribution of $\text{HC}_3\text{N}(38-37)$ to the CO(3–2) emission is also negligible.

4.3. Dense Molecular Gas Mass

In addition to $R_{\text{HCN}/\text{HCO}^+}$ and $R_{\text{HCN}/\text{CS}}$, we list line luminosities of HCN(4–3) and $\text{HCO}^+(4-3)$ extracted at position A and the whole CND (i.e., central $1''$ diameter region) in Table 4 as well since these lines are relatively strong enough to be detectable even in high-redshift galaxies (e.g., Barvainis et al. 1997; Riechers et al. 2011). By using these data, we roughly estimate the mass of dense molecular gas (M_{dense}) in the CND as follows. First, we convert $L'_{\text{HCN}(4-3)}$ to the corresponding value of HCN(1–0), assuming $\text{HCN}(4-3)/\text{HCN}(1-0) = 0.6 \pm 0.2$ in the brightness temperature unit. This ratio is an averaged value over the CND of the nearby typical Seyfert 2 galaxy, NGC 1068, sampled at 100 pc resolution (Viti et al. 2014). Note that NGC 1068 has a quite similar X-ray luminosity and Eddington ratio to NGC 7469. Then, we obtain $L'_{\text{HCN}(1-0)} = (9.3 \pm 3.1) \times 10^6 \text{ K km s}^{-1} \text{pc}^2$. Finally, assuming a conversion factor from $L'_{\text{HCN}(1-0)}$ to M_{dense} to be 10, which is derived for AGNs by Krips et al. (2008) based on IRAM 30 m observations, we estimate $M_{\text{dense}} = (9.3 \pm 3.1) \times 10^7 M_{\odot}$. The dynamical mass (M_{dyn}) of the CND, on the other hand, is calculated assuming a thin disk with Keplerian rotation as $M_{\text{dyn}} = 230 (r/\text{pc}) [v(r)^2/(\text{km s}^{-1})] (\sin i)^{-2} M_{\odot}$. Here $v(r)$ is a rotation velocity at a radius r , and i is an inclination angle of the disk. Then, putting the FWHM $\sim 200 \text{ km s}^{-1}$ at the CND ($1'' = 330$ pc diameter) and $i = 45^\circ$ (Davies et al. 2004), we obtain $M_{\text{dyn}} = 7.6 \times 10^8 M_{\odot}$. This is almost identical to the value derived in Fathi et al. (2015), who isolated the rotation velocity and the velocity dispersion based on their harmonic decomposition analysis of the observed velocity field. Our M_{dyn} is also consistent with those derived for the $r < 2''.5$ region, i.e., including the SB ring ($6.5 \times 10^9 M_{\odot}$; Davies et al. 2004).

Taking them together, we can estimate the dense gas mass fraction in the CND of NGC 7469 as $f_{\text{gas}} \equiv M_{\text{dense}}/M_{\text{dyn}} \sim 12\%$. Recalling the fact that the above-used mass conversion factor has a factor of ~ 3 uncertainty (Krips et al. 2008), f_{gas} eventually has the same level of uncertainty at this moment. Therefore, although the value of $f_{\text{gas}} \sim 12\%$ is comparable to those estimated for low-luminosity AGNs (Sani et al. 2012) using the same conversion factor (i.e., 10), it is still difficult to speculate whether or not f_{gas} has any relevance with the current mass accretion onto the central supermassive black hole. We need an accurate mass conversion factor estimated through multitransitional analysis (i.e., estimating an accurate relative abundance of HCN with respect to H_2) to further constrain the f_{gas} and its relevance to the nuclear activity.

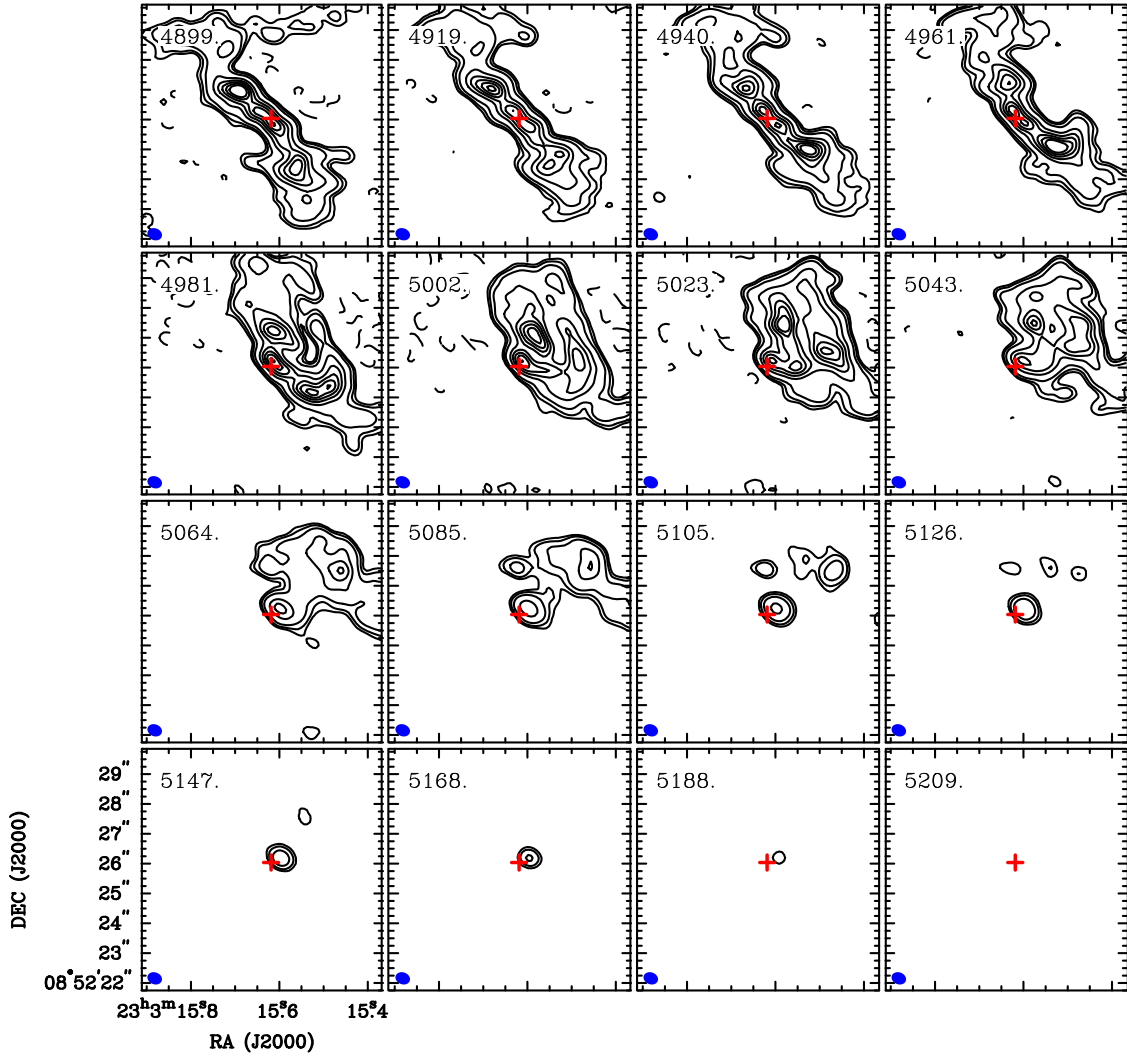


Figure 3. Velocity channel maps of the CO(3–2) line emission in the central $8'' \times 8''$ (2.6×2.6 kpc) region of NGC 7469. The central red plus sign in each channel indicates position A in Figure 1(a) (i.e., the AGN position). The velocity width of each channel is ~ 20 km s $^{-1}$, and the central velocity of each channel is shown in the upper left corner. The synthesized beam ($0''.50 \times 0''.40$, PA = $68^\circ 5$) is also plotted in the bottom left corner. Contour levels are -5σ , 3σ , 5σ , 10σ , 30σ , 50σ , 70σ , 90σ , and 110σ , where $1\sigma = 2.34$ mJy beam $^{-1}$. The negative contour is indicated by the dashed lines. Note that we could not observe channels with $V_{\text{LSR}} < 4900$ km s $^{-1}$ owing to our observational setup. Attenuation due to the primary beam pattern is corrected.

5. SPATIAL DISTRIBUTION OF THE DENSE GAS TRACERS

We show in Figures 3–5 the channel maps of the CO(3–2), HCN(4–3), and HCO $^+$ (4–3) line emissions from the central $8'' \times 8''$ (2.6×2.6 kpc) region of NGC 7469. We could not cover the whole CO(3–2) emission line as noted before. Comparing with the CO(2–1) map in Davies et al. (2004), we conclude that the emission from the southwest region of the map is missing. The HCN(4–3) and HCO $^+$ (4–3) emissions were detected (i.e., $>3\sigma$) over velocity ranges of 4744–5165 km s $^{-1}$ and 4752–5150 km s $^{-1}$ at position A, respectively, whose widths (FWZI ~ 400 km s $^{-1}$) are almost consistent with each other. As for CO(3–2), the covered velocity range corresponds to $\sim 70\%$ of the total velocity range of HCN(4–3) and HCO $^+$ (4–3) at position A. However, we cannot see a clear turnover feature in the CO(3–2) spectrum at that position (Figure 2). Therefore, we conclude that the FWZI of the CO(3–2) emission line is significantly wider than those of HCN(4–3) and HCO $^+$ (4–3) lines there. It might be possible

that we detected CO(3–2) emission from an outer diffuse, high-velocity component around the CND. It might also be possible that the high-velocity components of HCN(4–3) and HCO $^+$ (4–3) emission lines are too faint to be significantly detectable. On the other hand, the line widths at the knots of the SB ring are almost consistent among CO(3–2), HCN(4–3), and HCO $^+$ (4–3) emission lines (Figure 2). The channel maps also show that the CND and the SB ring are bridged by a bar-like or several spiral arm-like structures as morphologically discussed later. A detailed kinematic study of this region is presented in Fathi et al. (2015).

We also show the maps of the CO(3–2), HCN(4–3), HCO $^+$ (4–3), and CS(7–6) velocity-integrated intensities in the central 2 kpc region of NGC 7469 in Figure 6. The peak positions of the 860 μm continuum emission (positions A–D in Figure 1(a)) are again marked by the arrows in the CO(3–2) map. The dense gas tracers are also bright at these peak positions, indicating that they are the sites of dust-obscured star formation. Two rather fainter knots are also seen in the CO

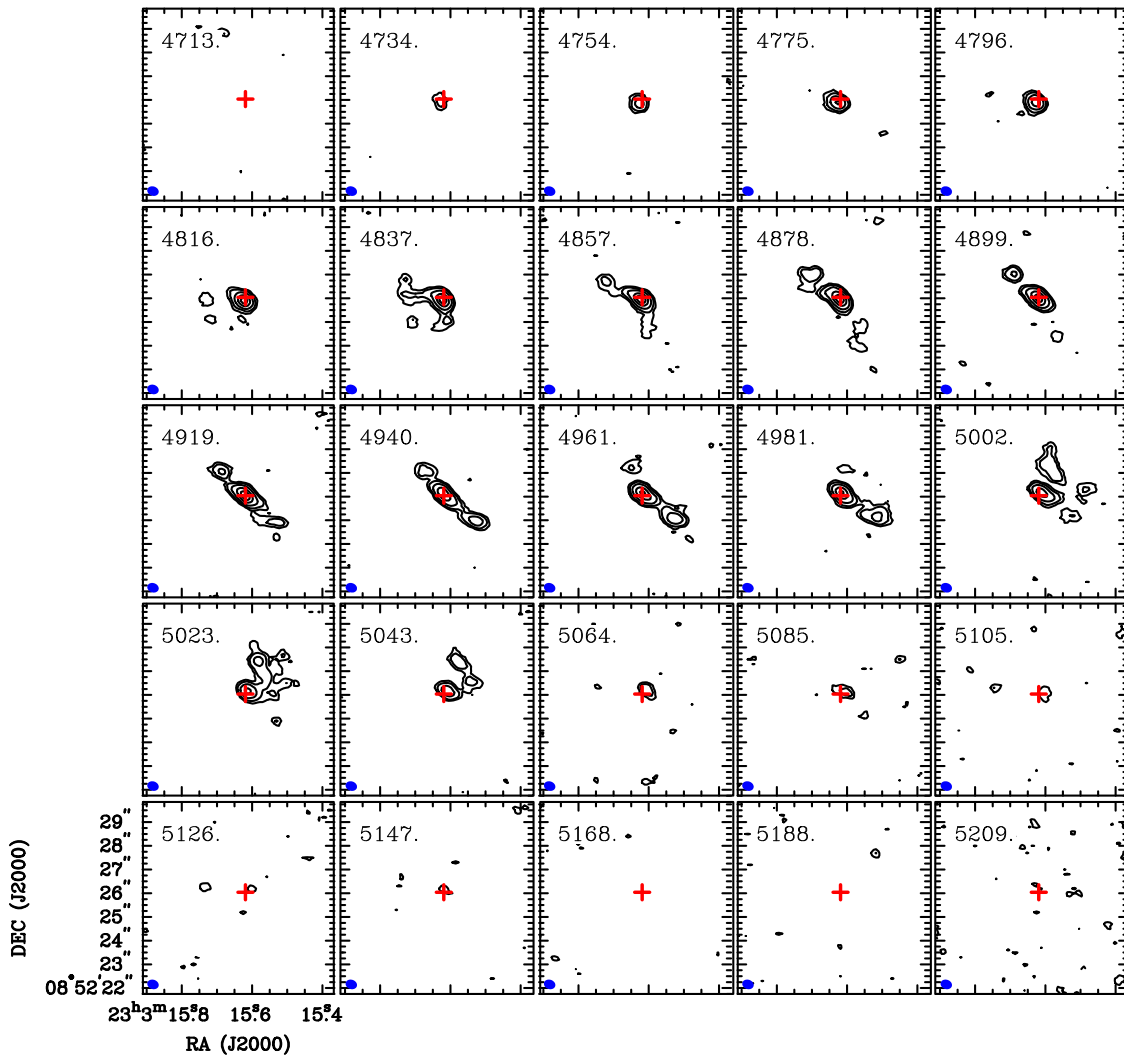


Figure 4. Velocity channel maps of the HCN(4–3) line emission in the central $8'' \times 8''$ (2.6×2.6 kpc) region of NGC 7469. The central red plus sign in each channel indicates position A in Figure 1(a) (i.e., the AGN position). The velocity width of each channel is ~ 20 km s $^{-1}$, and the central velocity of each channel is shown in the upper left corner. The synthesized beam ($0''.49 \times 0''.39$, PA = $70^\circ.4$) is also plotted in the bottom left corner. Contour levels are -5σ , 3σ , 5σ , 10σ , 20σ , and 30σ , where $1\sigma = 0.55$ mJy beam $^{-1}$. Although we set the negative contours to be indicated by the dashed lines, they are not prominent in this figure. Attenuation due to the primary beam pattern is corrected.

(3–2) map, which are located northwest of the CND (marked as E and F).

From these maps, it is apparent that the HCN(4–3), HCO $^+$ (4–3), and CS(7–6) emissions are significantly concentrated toward the CND. A two-dimensional Gaussian fit to the HCN(4–3) image shows that the CND has an extent of $(244.2 \pm 9.9) \times (194.7 \pm 6.6)$ pc 2 with PA = $58^\circ.8 \pm 6^\circ.7$, which is similar to that of HCO $^+$ (4–3) emission. This is the beam-convolved size; thus, the actual CND must be smaller. We derived these uncertainties using Monte Carlo techniques by creating 10^3 realizations of the image, each time adjusting the data by adding the normally distributed (measured) noise randomly. Again using Figure 6, we estimate that the CND of NGC 7469 contains $\sim 82\%$ and 53% of the total emission of HCN(4–3) and HCO $^+$ (4–3) within the $18''$ field of view of ALMA (~ 6 kpc), respectively, suggesting their utility to probe the nuclear regions of external galaxies especially about HCN(4–3).

Here we expect that the missing flux is not significant for the CND, although we recovered only $54\% \pm 16\%$ of the

HCO $^+$ (4–3) flux measured by APEX (Zhang et al. 2014) within the central $18''$ region, since its size ($\sim 1''$) is much smaller than that of the maximum measurable angular scale of our observations, which was $7''.1$ (2.3 kpc). Since the APEX’s HCO $^+$ (4–3) spectrum of Zhang et al. (2014) is somewhat noisy, we can expect that the systematic flux uncertainty would be larger than the value mentioned in that paper (15% for absolute flux calibration uncertainty) additionally owing to, e.g., baseline uncertainty. In other words, we expect that the actual recovered rate can be higher than 54%. Unfortunately, we cannot estimate the percentage of the recovered flux of HCN(4–3) and CS(7–6) since there is currently no significant detection of these line emissions with single-dish telescopes.

In addition to the CND, we can see a partial circumnuclear SB ring at a radius of $1''.5$ – $2''.5$. Davies et al. (2004) also reported the existence of a bar or a pair of short, loosely wound spiral arms at a PA = 56° between the CND and the SB ring (connecting positions B–A–D in Figure 6(a)), based on their $0''.7$ CO(2–1) observations. Interestingly, that structure is only found in molecular emission; neither *K*-band (Genzel

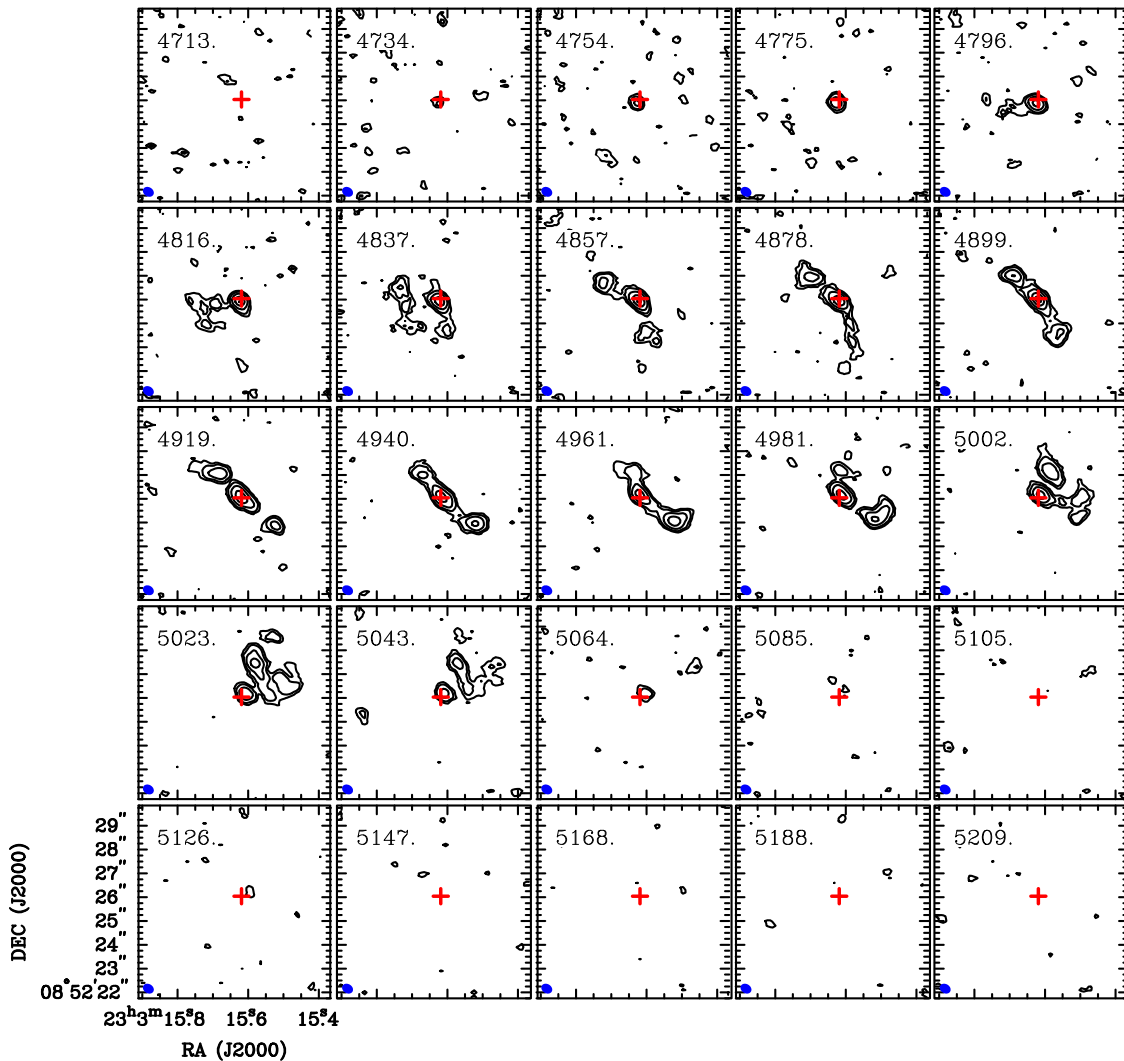


Figure 5. Velocity channel maps of the $\text{HCO}^+(4-3)$ line emission in the central $8'' \times 8''$ (2.6×2.6 kpc) region of NGC 7469. The central red plus sign in each channel indicates position A in Figure 1(a) (i.e., the AGN position). The velocity width of each channel is $\sim 20 \text{ km s}^{-1}$, and the central velocity of each channel is shown in the upper left corner. The synthesized beam ($0''.48 \times 0''.38$, $\text{PA} = 57^\circ.9$) is also plotted in the bottom left corner. Contour levels are -5σ , 3σ , 5σ , 10σ , 20σ , and 30σ , where $1\sigma = 0.58 \text{ mJy beam}^{-1}$. Although we set the negative contours to be indicated by the dashed lines, they are not prominent in this figure. Attenuation due to the primary beam pattern is corrected.

et al. 1995; Scoville et al. 2000) nor centimeter continuum (Condon et al. 1991; Orienti & Prieto 2010) images show such a structure. This configuration is quite unusual if the structure is a genuine molecular bar, since a corresponding stellar structure should be easily visible in this scenario. Indeed, Davies et al. (2004) found no kinematic characteristics expected for a barred potential, i.e., an S-shaped contour in an isovelocity field (e.g., Kohno et al. 1999; Lundgren et al. 2004) and a tilted-X shape in a position–velocity diagram along the (hypothesized) bar axis (e.g., Laine et al. 1999; Sakamoto et al. 2000). Moreover, Figures 4 and 5 reveal that there seem to be several connections between the CND and the SB ring in addition to the above hypothesized bar axis, e.g., channels at around 4850, 4980, and 5020 km s^{-1} . Although we cannot rule out the existence of a faint stellar bar that could not be detected in previous NIR observations, it might be possible that the nuclear region of NGC 7469 consists of several spiral features like the case of, e.g., NGC 1097 (Prieto et al. 2005; Fathi et al. 2006; Davies et al. 2009). Since the lack of spatial resolution leads to blending several molecular clouds, which would result in an

illusional bar, higher angular resolution and sensitivity observations of both CO and NIR emissions are necessary to settle this issue.

6. SUMMARY AND CONCLUSION

In this paper, we present high-resolution ($0''.5 \times 0''.4$; $1'' = 330 \text{ pc}$) ALMA band 7 (350 GHz band) observations of the submillimeter dense molecular gas tracers such as $\text{HCN}(4-3)$, $\text{HCO}^+(4-3)$, $\text{CS}(7-6)$, and partially $\text{CO}(3-2)$, in addition to the underlying $860 \mu\text{m}$ continuum emission, toward the central kiloparsec region of the luminous type 1 Seyfert galaxy NGC 7469. The region consists of the CND (central $\sim 1''$) and the surrounding SB ring with a radius of $1''.5-2''.5$. We revealed the spatial distribution of these emissions. Thanks to the high spatial resolution, we can reliably measure the line fluxes at the CND and the SB ring separately. The obtained line ratios are directly compared with those in NGC 1097 (a low-luminosity type 1 Seyfert galaxy), to achieve insights of possible effects of AGN luminosity on the surrounding

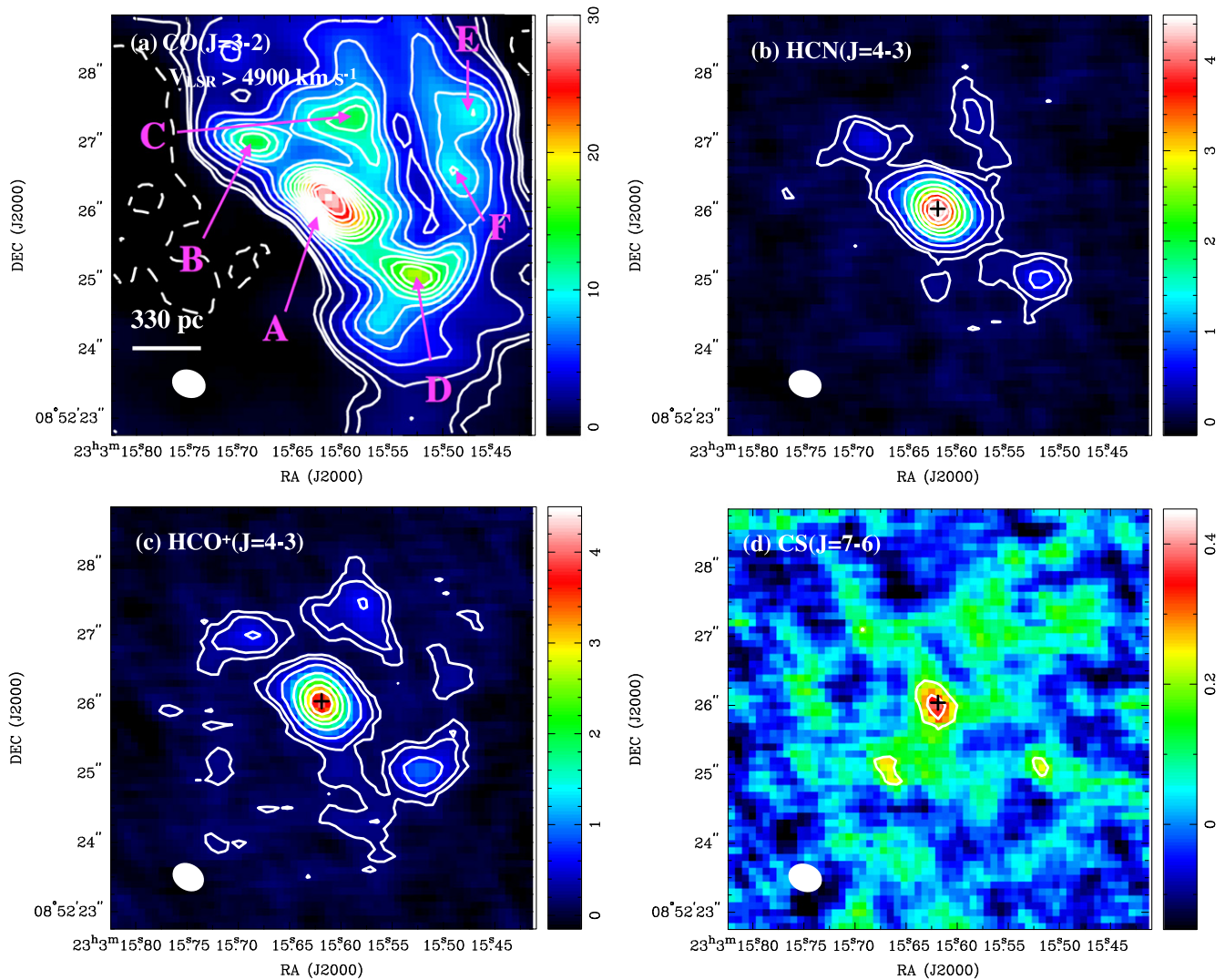


Figure 6. Integrated intensity maps of (a) CO(3–2), (b) HCN(4–3), (c) HCO⁺(4–3), and (d) CS(7–6), in the central ~ 2 kpc region of NGC 7469. The rms noises (1σ) are 0.20, 0.06, 0.06, and 0.06 Jy beam⁻¹ km s⁻¹ in (a)–(d), respectively. Note that we could not observe CO(3–2) emission at $V_{\text{LSR}} < 4900$ km s⁻¹ owing to our observational setting; thus, the displayed map is incomplete (southeast part is deficient). Some bright molecular knots are marked as A–F in the CO(3–2) map (positions A–D are the same as the ones marked in Figure 1(a)). The white filled ellipses indicate the synthesized beams ($\sim 0''.50 \times 0''.40$). The central plus signs indicate the AGN position. Contours are (a) -5σ , 3σ , 5σ , 10σ , 20σ , 30σ , ..., and 130σ ; (b) -5σ , 3σ , 5σ , 10σ , 20σ , 30σ , ..., and 70σ ; (c) -5σ , 3σ , 5σ , 10σ , 20σ , 30σ , 40σ , and 50σ ; and (d) -5σ , 3σ , and 5σ , respectively. Negative contours are indicated by dashed lines. See also Section 2 for the velocity ranges integrated over.

molecular material. The main results of our observations and conclusions are summarized as follows:

1. The spatial distribution of the $860 \mu\text{m}$ continuum emission resembles well those of centimeter and MIR continuum emissions and dense molecular gas tracers. But their peak positions (including some knots in the SB ring) are shifted significantly from the optical ones, suggesting the existence of dust-obscured star formation there.
2. The maximum position of the $860 \mu\text{m}$ continuum is identical to that of the VLA 8.4 GHz continuum, indicating that it is the AGN position. The SED reveals that the $860 \mu\text{m}$ continuum there is dominated by a thermal dust emission. We detected CO(3–2), HCN(4–3), HCO⁺(4–3), and CS(7–6) emissions at the same position. Other lines including the vibrationally excited HCN were not detected, although NGC 7469 is classified as a LIRG.
3. The high $R_{\text{HCN}/\text{HCO}^+}$ and $R_{\text{HCN}/\text{CS}}$ are only found in the CND, which is consistent with the findings in I13, i.e., AGNs tend to show higher $R_{\text{HCN}/\text{HCO}^+}$ ($\gtrsim 1$) and/or $R_{\text{HCN}/\text{CS}}$ ($\gtrsim 10$) than those in SB galaxies (submillimeter-HCN enhancement).
4. Although the actual physical mechanisms to enhance $R_{\text{HCN}/\text{HCO}^+}$ in AGNs are still unclear, we found that this ratio is significantly lower in NGC 7469 (1.11 ± 0.13) than in NGC 1097 (2.0 ± 0.2) despite the more than two orders of magnitude higher X-ray luminosity of NGC 7469 than that of NGC 1097. The close vicinity of the luminous AGN of NGC 1068 also shows a comparable ratio (~ 1.5) to NGC 7469. Some other heating mechanisms than X-ray (e.g., mechanical heating) would contribute significantly for shaping the chemical composition in NGC 1097.
5. The CO(3–2) emission, which is not fully observed though, is distributed over both the CND and the SB ring,

whereas the HCN(4–3) and the HCO⁺(4–3) emissions are significantly concentrated toward the CND ($\sim 82\%$ and 53% of the total flux inside the $18''$ field of view of ALMA, for HCN and HCO⁺, respectively), suggesting their utility to probe the nuclear regions of galaxies.

6. Between the CND and the SB ring, we found several spiral-like structures, which would be transporting gas from the SB ring to the CND. This might be a more preferable scenario than a bar. We should test this tentative view by further high-resolution observations and kinematic analysis.

From this work, we achieved supportive evidence for the submillimeter-HCN enhancement in AGNs tentatively proposed by I13. We will further investigate this trend by increasing the number of sample galaxies and will extensively discuss the possible cause of the HCN enhancement in our succeeding paper (Izumi et al. 2015).

We thank the anonymous referee for very kind and helpful comments for improving the paper. This paper makes use of the following ALMA data: ADS/JAO.ALMA#2012.1.00165.S. ALMA is a partnership of ESO (representing its member states), NSF (USA), and NINS (Japan), together with NRC (Canada) and NSC and ASIAA (Taiwan), in cooperation with the Republic of Chile. The Joint ALMA Observatory is operated by ESO, AUI/NRAO, and NAOJ. The National Radio Astronomy Observatory is a facility of the National Science Foundation operated under cooperative agreement by Associated Universities, Inc. We used data based on observations with the NASA/ESA *Hubble Space Telescope* and obtained from the Hubble Legacy Archive, which is a collaboration between the Space Telescope Science Institute (STScI/NASA), the Space Telescope European Coordinating Facility (ST-ECF/ESA), and the Canadian Astronomy Data Centre (CADC/NRC/CSA). In addition, this research has made use of the NASA/IPAC Extragalactic Database (NED), which is operated by the Jet Propulsion Laboratory, California Institute of Technology, under contract with the National Aeronautics and Space Administration. T.I. was supported by the ALMA Japan Research Grant of NAOJ Chile Observatory, NAOJ-ALMA-0029. T.I. and H.U. are thankful for the fellowship received from the Japan Society for the Promotion of Science (JSPS).

APPENDIX A THE SIZE OF AN XDR

Here we estimate the size of an XDR, which is defined as the largest distance from an AGN where X-ray heating due to the AGN dominates over UV heating due to SB, by employing a toy model.

For the X-ray incident flux, we adopt a spectral shape of the form

$$F(E) = F_0 \left(\frac{E}{1 \text{ keV}} \right)^{-\alpha} \exp(-E/E_c), \quad (1)$$

where F_0 is a scaling constant, $E = h\nu$ eV, α is a power-law index, and E_c is a cutoff energy. We set $\alpha = 1.0$ (e.g., Madejski et al. 1995; Peterson 1997) and $E_c = 100$ keV (e.g., Madejski et al. 1995). We hereafter consider the 1–10 keV photons for simplicity. The softer X-ray can be easily absorbed at the edge of the molecular cloud and thus neglected here. Considering the

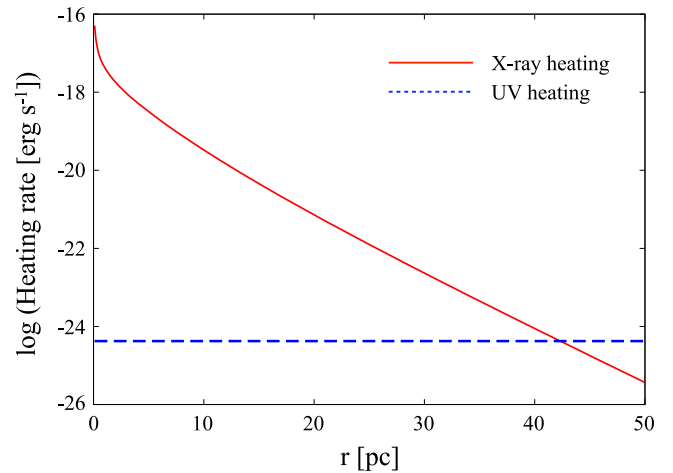


Figure 7. Heating rate per hydrogen atom due to X-ray absorption (red solid) and to soft-UV absorption (blue dashed) as a function of radius from the center, under the 1D slab geometry. We assume that an $M_{\text{BH}} = 10^7 M_{\odot}$ black hole is emitting 3% of its Eddington luminosity at 1–10 keV. The soft-UV radiation field is taken as $G_0 = 10^{2.5}$ (Habing unit). The adopted gas density is $n_{\text{H}} = 10^5 \text{ cm}^{-3}$. In this configuration, the estimated size of the XDR is $r \sim 42$ pc.

situation that an AGN with $r = 0.1$ pc and $M_{\text{BH}} = 10^7 M_{\odot}$ is emitting isotropically at 3% of its Eddington luminosity at this 1–10 keV range, we scaled F_0 . Subsequent radiative transfer is calculated by adopting a 1D slab geometry with a uniform gas density of $n_{\text{H}} = 10^5 \text{ cm}^{-3}$. Note that the AGN of NGC 7469 hosts a $\sim 10^7 M_{\odot}$ black hole with the Eddington ratio of ~ 0.3 (see also Section 1). Thus, our estimation corresponds to the case where 10% of the bolometric AGN luminosity of NGC 7469 is going into the 1–10 keV band. Then, an energy deposition rate per particle (H_{X} ; Maloney et al. 1996) is

$$H_{\text{X}} = \int_{1 \text{ keV}}^{10 \text{ keV}} \sigma_{\text{pa}}(E) F(E) \exp(-\tau) dE, \quad (2)$$

with an optical depth of

$$\tau = \sigma_{\text{pa}}(E) \cdot N_{\text{H}}(r). \quad (3)$$

Here we use the photoelectric absorption cross section $\sigma_{\text{pa}}(E)$ of Morrison & McCammon (1983), which is estimated for the 1–10 keV range. The attenuating hydrogen column density from the AGN to the point at the distance of r pc is indicated by N_{H} . Assuming the heating efficiency of X-ray photons to be 30% (e.g., Maloney et al. 1996; Meijerink & Spaans 2005), an X-ray heating rate is calculated as a function of a radius from the AGN (Figure 7). On the other hand, we adopt a typical energy of 10 eV and a cross section of $2.78 \times 10^{-22} \text{ cm}^2$ for soft-UV photons from the SB activity (Meijerink & Spaans 2005). This SB is assumed to produce a soft-UV radiation field of $G_0 = 10^{2.5}$ (Habing unit). Note that Rosenberg et al. (2014a, 2014b) used this G_0 to reproduce $J_{\text{upper}} \lesssim 4$ ¹²CO emission lines (i.e., lines tracing cold molecular gas) observed in NGC 253 and Arp 299. Assuming that the UV heating efficiency is $\sim 0.3\%$, the heating rate due to SB-induced UV radiation is also shown in Figure 7.

Although the above estimation strongly depends on the adopted parameters and the value of G_0 is not well constrained in the circumnuclear region of Seyfert galaxies at this moment,

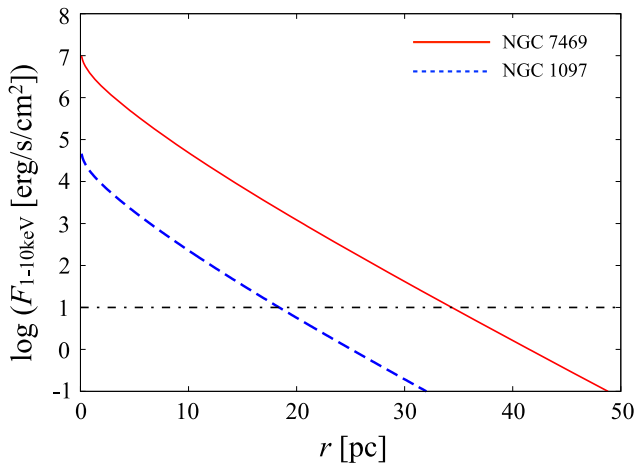


Figure 8. 1D calculation of the 1–10 keV X-ray flux as a function of radius from the AGN. Attenuation due to obscuring material (Morrison & McCammon 1983) is taken into account. The cases of NGC 7469 (red solid) and NGC 1097 (blue dashed) are shown. The horizontal dot-dashed line indicates the flux of $10 \text{ erg s}^{-1} \text{ cm}^{-2}$, which is a required value by Meijerink et al. (2007) to realize $R_{\text{HCN}/\text{HCO}^+} > 1$. Thus, the largest radius that can keep $F_{1-10 \text{ keV}} \geq 10$ is $\sim 35 \text{ pc}$ and $\sim 18 \text{ pc}$ for NGC 7469 and NGC 1097, respectively.

we can roughly estimate the size of the XDR from Figure 7, which is $r \sim 42 \text{ pc}$ in this case. This size is well smaller than the spatial resolution of our ALMA observations (150 pc).

APPENDIX B ATTENUATED X-RAY FLUX

Using Equations (1) and (3), we can calculate an attenuated 1–10 keV X-ray flux as a function of radius. The cases of NGC 7469 and NGC 1097 are investigated. Again we used the photoelectric absorption cross section calculated by Morrison & McCammon (1983). We adopt the same values as indicated in Appendix A for this calculation, except for F_0 . In this time, we scaled F_0 by using the 2–10 keV luminosity of NGC 7469 and NGC 1097 (e.g., Liu et al. 2014), $\alpha = 1.0$, and assuming their AGN sizes to be $r = 0.1 \text{ pc}$. Then, the attenuated X-ray flux is shown in Figure 8.

REFERENCES

Alberdi, A., Colina, L., Torrelles, J. M., et al. 2006, *ApJ*, 638, 938
 Barvainis, R., Maloney, P., Antonucci, R., & Alloin, D. 1997, *ApJ*, 484, 695
 Blustin, A. J., Kriss, G. A., Holczer, T., et al. 2007, *A&A*, 466, 107
 Bonatto, C. J., & Pastoriza, M. G. 1990, *ApJ*, 353, 445
 Colina, L., Alberdi, A., Torrelles, J. M., Panagia, N., & Wilson, A. S. 2001, *ApJL*, 553, L19
 Collier, S. J., Horne, K., Kaspi, S., et al. 1998, *ApJ*, 500, 162
 Combes, F., García-Burillo, S., Casasola, V., et al. 2013, *A&A*, 558, A124
 Combes, F., García-Burillo, S., Casasola, V., et al. 2014, *A&A*, 565, A97
 Condon, J. J., Huang, Z.-P., Yin, Q. F., & Thuan, T. X. 1991, *ApJ*, 378, 65
 Davies, R. I., Maciejewski, W., Hicks, E. K. S., et al. 2009, *ApJ*, 702, 114
 Davies, R. I., Müller Sánchez, F., Genzel, R., et al. 2007, *ApJ*, 671, 1388
 Davies, R. I., Tacconi, L. J., & Genzel, R. 2004, *ApJ*, 602, 148
 Díaz, A. I., Álvarez, M. Á., Terlevich, E., et al. 2000, *MNRAS*, 311, 120
 Díaz-Santos, T., Alonso-Herrero, A., Colina, L., Ryder, S. D., & Knapen, J. H. 2007, *ApJ*, 661, 149
 Fathi, K., Izumi, T., Romeo, A. B., et al. 2015, *ApJL*, 806, L34
 Fathi, K., Lundgren, A. A., Kohno, K., et al. 2013, *ApJL*, 770, L27
 Fathi, K., Storchi-Bergmann, T., Riffel, R. A., et al. 2006, *ApJL*, 641, L25
 Gao, Y., & Solomon, P. M. 2004a, *ApJS*, 152, 63
 Gao, Y., & Solomon, P. M. 2004b, *ApJ*, 606, 271

García-Burillo, S., Combes, F., Usero, A., et al. 2014, *A&A*, 567, A125
 García-Burillo, S., Usero, A., Fuente, A., et al. 2010, *A&A*, 519, A2
 Genzel, R., Weitzel, L., Tacconi-Garman, L. E., et al. 1995, *ApJ*, 444, 129
 Gorjian, V., Werner, M. W., Jarrett, T. H., Cole, D. M., & Ressler, M. E. 2004, *ApJ*, 605, 156
 Greve, T. R., Papadopoulos, P. P., Gao, Y., & Radford, S. J. E. 2009, *ApJ*, 692, 1432
 Harada, N., Herbst, E., & Wakelam, V. 2010, *ApJ*, 721, 1570
 Harada, N., Thompson, T. A., & Herbst, E. 2013, *ApJ*, 765, 108
 Henkel, C., Asiri, H., Ao, Y., et al. 2014, *A&A*, 565, A3
 Hicks, E. K. S., Davies, R. I., Malkan, M. A., et al. 2009, *ApJ*, 696, 448
 Hollenbach, D. J., & Tielens, A. G. G. M. 1999, *RvMP*, 71, 173
 Imanishi, M., & Wada, K. 2004, *ApJ*, 617, 214
 Israel, F. P. 2009, *A&A*, 493, 525
 Israel, F. P., White, G. J., & Baas, F. 1995, *A&A*, 302, 343
 Izumi, T., Kohno, K., Martín, S., et al. 2013, *PASJ*, 65, 100
 Izumi, T., Kohno, K., Aalto, S., et al. 2015, *ApJ*, submitted
 Kazandjian, M. V., Meijerink, R., Pelupessy, I., Israel, F. P., & Spaans, M. 2012, *A&A*, 542, A65
 Kazandjian, M. V., Meijerink, R., Pelupessy, I., Israel, F. P., & Spaans, M. 2015, *A&A*, 574, A127
 Knapen, J. H., Shlosman, I., & Peletier, R. F. 2000, *ApJ*, 529, 93
 Knudsen, K. K., Walter, F., Weiss, A., et al. 2007, *ApJ*, 666, 156
 Kohno, K., Kawabe, R., & Vila-Vilaró, B. 1999, *ApJ*, 511, 157
 Krips, M., Martín, S., Eckart, A., et al. 2011, *ApJ*, 736, 37
 Krips, M., Neri, R., García-Burillo, S., et al. 2008, *ApJ*, 677, 262
 Kriss, G. A., Peterson, B. M., Crenshaw, D. M., & Zheng, W. 2000, *ApJ*, 535, 58
 Laine, S., Kenney, J. D. P., Yun, M. S., & Gottesman, S. T. 1999, *ApJ*, 511, 709
 Lepp, S., & Dalgarno, A. 1996, *A&A*, 306, L21
 Liu, T., Wang, J.-X., Yang, H., Zhu, F.-F., & Zhou, Y.-Y. 2014, *ApJ*, 783, 106
 Lonsdale, C. J., Lonsdale, C. J., Smith, H. E., & Diamond, P. J. 2003, *ApJ*, 592, 804
 Lundgren, A. A., Olofsson, H., Wiklind, T., & Rydbeck, G. 2004, *A&A*, 422, 865
 Madejski, G. M., Zdziarski, A. A., Turner, T. J., et al. 1995, *ApJ*, 438, 672
 Malkan, M. A., Gorjian, V., & Tam, R. 1998, *ApJS*, 117, 25
 Maloney, P. R., Hollenbach, D. J., & Tielens, A. G. G. M. 1996, *ApJ*, 466, 561
 Marquez, I., & Moles, M. 1994, *AJ*, 108, 90
 Martín, S., Aladro, R., Martín-Pintado, J., & Mauersberger, R. 2010, *A&A*, 522, A62
 Martín, S., Kohno, K., Izumi, T., et al. 2015, *A&A*, 573, A116
 Martín, S., Martín-Pintado, J., & Mauersberger, R. 2009, *ApJ*, 694, 610
 Matsushita, S., Trung, D.-V., Boone, F., et al. 2015, *ApJ*, 799, 26
 McMullin, J. P., Waters, B., Schiebel, D., Young, W., & Golap, K. 2007, in ASP Conf. Ser. 376, *Astronomical Data Analysis Software and Systems XVI*, ed. R. A. Shaw, F. Hill & D. J. Bell (San Francisco, CA: ASP), 127
 Meijerink, R., & Spaans, M. 2005, *A&A*, 436, 397
 Meijerink, R., Spaans, M., & Israel, F. P. 2006, *ApJL*, 650, L103
 Meijerink, R., Spaans, M., & Israel, F. P. 2007, *A&A*, 461, 793
 Meijerink, R., Spaans, M., Loenen, A. F., & van der Werf, P. P. 2011, *A&A*, 525, A119
 Meixner, M., Puchalsky, R., Blitz, L., Wright, M., & Heckman, T. 1990, *ApJ*, 354, 158
 Mezcuca, M., & Prieto, M. A. 2014, *ApJ*, 787, 62
 Morrison, R., & McCammon, D. 1983, *ApJ*, 270, 119
 Müller-Sánchez, F., Prieto, M. A., Hicks, E. K. S., et al. 2011, *ApJ*, 739, 69
 Nakajima, T., Takano, S., Kohno, K., et al. 2015, *PASJ*, 67, 8
 Nandra, K., Le, T., George, I. M., et al. 2000, *ApJ*, 544, 734
 Orienti, M., & Prieto, M. A. 2010, *MNRAS*, 401, 2599
 Osterbrock, D. E., & Martel, A. 1993, *ApJ*, 414, 552
 Panessa, F., Bassani, L., Cappi, M., et al. 2006, *A&A*, 455, 173
 Papadopoulos, P. P., & Allen, M. L. 2000, *ApJ*, 537, 631
 Perez-Olea, D. E., & Colina, L. 1996, *ApJ*, 468, 191
 Peterson, B. M. 1997, *An Introduction to Active Galactic Nuclei* (Cambridge: Cambridge Univ. Press)
 Peterson, B. M., Ferrarese, L., Gilbert, K. M., et al. 2004, *ApJ*, 613, 682
 Peterson, B. M., Grier, C. J., Horne, K., et al. 2014, *ApJ*, 795, 149
 Petrucci, P. O., Maraschi, L., Haardt, F., & Nandra, K. 2004, *A&A*, 413, 477
 Prieto, M. A., Maciejewski, W., & Reunanen, J. 2005, *AJ*, 130, 1472
 Reunanen, J., Prieto, M. A., & Siebenmorgen, R. 2010, *MNRAS*, 402, 879
 Riechers, D. A., Walter, F., Carilli, C. L., et al. 2011, *ApJ*, 726, 50
 Rosenberg, M. J. F., Kazandjian, M. V., van der Werf, P. P., et al. 2014a, *A&A*, 564, A126
 Rosenberg, M. J. F., Meijerink, R., Israel, F. P., et al. 2014b, *A&A*, 568, A90

- Rosenberg, M. J. F., van der Werf, P. P., Aalto, S., et al. 2015, *ApJ*, **801**, 72
- Sakamoto, K., Baker, A. J., & Scoville, N. Z. 2000, *ApJ*, **533**, 149
- Sakamoto, K., Mao, R.-Q., Matsushita, S., et al. 2011, *ApJ*, **735**, 19
- Salpeter, E. E. 1955, *ApJ*, **121**, 161
- Sanders, D. B., Mazzarella, J. M., Kim, D.-C., Surace, J. A., & Soifer, B. T. 2003, *AJ*, **126**, 1607
- Sanders, D. B., Soifer, B. T., Scoville, N. Z., & Sargent, A. I. 1988, *ApJL*, **324**, L55
- Sani, E., Davies, R. I., Sternberg, A., et al. 2012, *MNRAS*, **424**, 1963
- Sault, R. J., Teuben, P. J., & Wright, M. C. H. 1995, in ASP Conf. Ser. 77, *Astronomical Data Analysis Software and Systems IV*, ed. R. A. Shaw, H. E. Payne & J. J. E. Hayes (San Francisco, CA: ASP), 433
- Schilke, P., Groesbeck, T. D., Blake, G. A., & Phillips, T. G. 1997, *ApJS*, **108**, 301
- Scott, J. E., Kriss, G. A., Lee, J. C., et al. 2005, *ApJ*, **634**, 193
- Scoville, N. Z., Evans, A. S., Thompson, R., et al. 2000, *AJ*, **119**, 991
- Shankar, F., Weinberg, D. H., & Miralda-Escudé, J. 2009, *ApJ*, **690**, 20
- Soifer, B. T., Bock, J. J., Marsh, K., et al. 2003, *AJ*, **126**, 143
- Solomon, P. M., & Vanden Bout, P. A. 2005, *ARA&A*, **43**, 677
- Takano, S., Nakajima, T., Kohno, K., et al. 2014, *PASJ*, **66**, 75
- van der Tak, F. F. S., Black, J. H., Schöier, F. L., Jansen, D. J., & van Dishoeck, E. F. 2007, *A&A*, **468**, 627
- Viti, S., García-Burillo, S., Fuente, A., et al. 2014, *A&A*, **570**, A28
- Wilson, A. S., Helfer, T. T., Haniff, C. A., & Ward, M. J. 1991, *ApJ*, **381**, 79
- Zhang, Z.-Y., Gao, Y., Henkel, C., et al. 2014, *ApJL*, **784**, L31